SOME RECENT RESULTS FROM CLEO II

Richard Kass*
Department of Physics
The Ohio State University, Columbus Ohio 43210

Representing the CLEO Collaboration

ABSTRACT

The CLEO experiment has been operating for several years now collecting e^+e^- annihilation data at and near the $\Upsilon(4S)$ resonance ($E_{cm} \approx 10.6$ GeV). The accumulated event sample contains several million $B\bar{B}$ and $\tau^+\tau^-$ pairs. This data is used to explore rare b, c and τ decays. In this report several recent CLEO results in the area of B-meson and τ decay are presented. The topics covered include: penguin decays of B-mesons, measurement of exclusive $b \to u$ semileptonic transitions, τ decays with an η in the final state, precision measurement of the Michel parameters in leptonic τ decay, and a search for lepton number violation using τ's.

*Supported by DOE grant DE-FG02-91ER40690.

1 Introduction

In this report B-meson and τ lepton physics results from the CLEO collaboration will be discussed. The CLEO experiment occupies the sole interaction region at the Cornell Electron-Positron Storage Ring (CESR). To date, CLEO has collected a total integrated luminosity in excess of 5 fb^{-1}, with $\approx$ two thirds of the data collected at the Υ(4S) ($\sqrt{s}$ =10.58 GeV),[1] and the rest at energies slightly below the Υ(4S). This luminosity corresponds to the production of $\approx 3\times10^6$ $B\bar{B}$ and 5×10^6 τ-pairs.

The CLEO-II detector,[2] shown in Fig. 1, emphasizes precision charged particle tracking, high resolution electromagnetic calorimetry, and good lepton identification. The various subsystems that make up the detector are described in Table 1. All detector subsystems, with the exception of the muon chambers reside in a 1.5 T solenoidal magnetic field. The momentum of a charged particle is measured by reconstructing its trajectory as it traverses the three drift chamber systems (PTL,VD, DR). The energy and angle of electrons and photons is measured using a calorimeter (BCC, ECC) that consists of $\approx$ 8000 CsI crystals.

The identification of electrons is primarily accomplished by comparing the momentum measured by the drift chamber with the energy measured in the CsI calorimeter. Muons are identified by their ability to penetrate a significant amount of iron without undergoing an inelastic collision. Thus charged particles which traverse the drift chambers, calorimeter, magnet iron, and match up with hits in the muon chambers are labeled muons. The lepton identification efficiencies and fake rates are summarized in Table 2. Finally, charged hadrons (π, K, p) are identified over a limited momentum region using an array of scintillation counters to measure their time of flight and the main drift chamber to measure their average ionization energy loss (dE/dx).

2 B-meson Physics

The production and subsequent decay of the Υ(4S) provides the B-mesons for the CLEO experiment. This source of B-mesons has several attractive features for the experimentalist including:

- The Υ(4S) decays exclusively into a pair of B-mesons, no extra particles are produced.

Table 1: The detector subsystems of the CLEO detector.

Device	#	R(cm)	$\|z\|$(cm)	$\|cos\theta\|$	Resolution
PTL	6	4.7-7.2	25	0.96	50μm (DME @ 6 mm H_2O)
Inner VD Cath	1	7.6	19	0.92	1.3 mm (5.85 mm strips)
VD	10	8.5-16	35	0.91	90μm (Ar/Et @ 6 PSIG)
Outer VD Cath	1	17.1	33	0.90	1.3 mm (6.85 mm strips)
Inner DR Cath	1	18.6	48	0.92	1.3 mm (1cm strips)
DR	1	19.9-90.1	97	0.71	120μm (Ar/Et @6 mm H_2O)
Outer DR Cath	1	96.1	91	0.71	1.3 mm (1cm strips)
Combined CD	67/4	47-90.1	-	0.92	$\sigma_p/p(\%) = \sqrt{(0.15p)^2 + 0.5^2}$
					$\sigma_{dE/dx}(e) = 6.3\%$ @ 5 GeV
TF-Barrel	64	96-101	140	0.77	$\sigma_t(\pi)$ =154 ps
					2σ $\pi - K$ for p_t <1.1 GeV/c
TF-Endcap	2x28	31-89	120-125	0.81-0.96	$\sigma_t(\pi)$ =240 ps
CC-Barrel	6144	102-132	167	0.82	$\frac{\sigma_E}{E}(\%) = \frac{0.35}{E^{-0.75}} + 1.9 - 0.1E$
					σ_ϕ(mrad)=$2.8/\sqrt{E}$+1.9
CC-Endcap	2x828	33-91	125-155	0.81-0.98	$\sigma_E/E(\%) = 0.26/E + 2.5$
Mu-Barrel	3	210,246,282	240	0.71	$\approx$4 cm @ 5GeV
Mu-Endcap	2x1	160-310	280	0.67-0.85	$\approx$5 cm @ 5GeV

Table 2: Lepton identification efficiencies and fake rates.

Lepton	p (GeV)	$\epsilon(\%)$	Fake rate/track (%)
electron	0.4-5.3	95	0.3
muon	1.5-2.1	70-93	$0.7(\pi)/1.0(K)$
	2.1-5.3	93	$1.2(\pi)/1.7(K)$

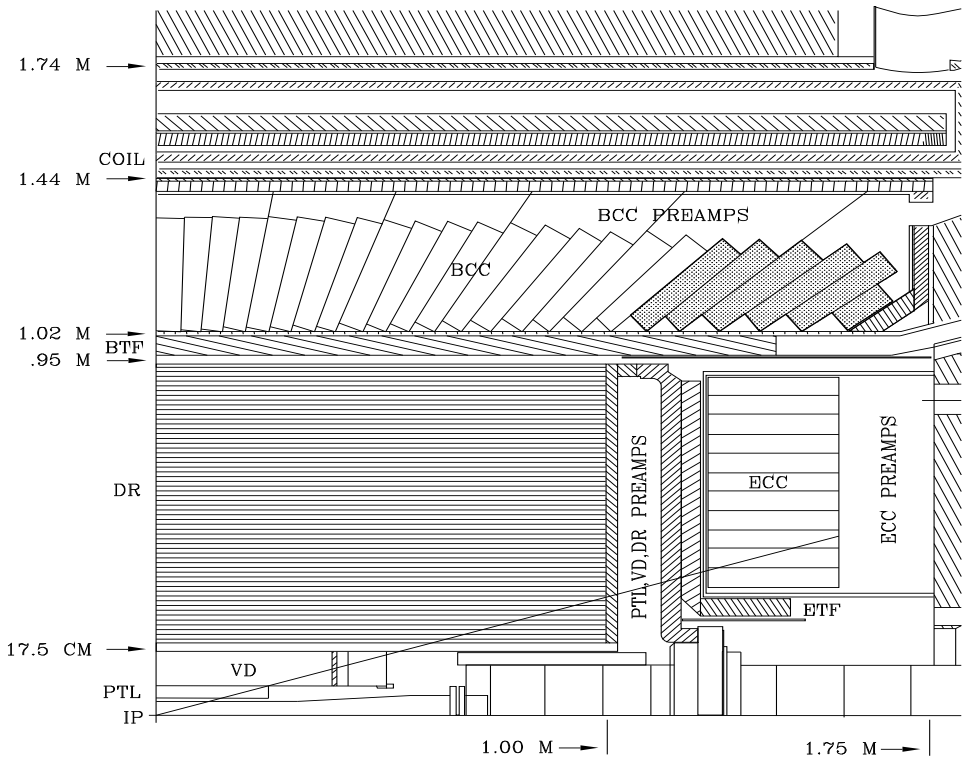

Figure 1: Quarter section of the CLEO II detector.

- To the accuracy that it can be measured $B^o\bar{B}^o$ and B^+B^- pairs are produced in equal numbers.
- The energy of a B-meson is given by the CESR beam energy and hence is determined to a higher accuracy than if it were to be measured by CLEO.
- The mass resolution of a B meson is improved by using the beam energy in place of the measured energy of a B candidate, i.e. $M_B = \sqrt{E_{beam}^2 - p^2}$, with p the measured momentum of the B decay products.
- A B-meson free sample of data can be obtained by running CESR at a center of mass energy below the mass of the Υ(4S).
- The cross section for producing B-mesons from the decay of the Υ(4S) is about 1/3 the continuum hadronic cross section ($e^+e^- \rightarrow q\bar{q}$).

The fact that $m_{\Upsilon(4S)} \approx 2m_B$ is a mixed blessing. Since the B's are practically at rest ($\beta \approx 0.06$) when they decay the particles produced in these events tend to populate the detector in an isotropic fashion. This is in contrast to the 'jet-like' structure of events produced via $e^+e^- \rightarrow q\bar{q}$. This difference in event shape can

be exploited when a B-meson rich event sample is desired.

There are however two drawbacks to having the B's decay at rest. First, since the particles tend to be produced isotopically, it is very difficult to associate a given particle with its parent B. This is in contrast to the situation at LEP and/or SLC where the B decay products tend to follow the direction of the parent B. Second, the mean decay length of a B is $\approx 30\mu$m, too short for silicon vertex detectors to separate the primary and secondary vertices. Again, this is in contrast to the situation at LEP/SLC where the mean decay length is several mm.

2.1 $B^o \to D^{(*)+}D^{(*)-}$

Two body decays of the form $B^o \to D^{(*)+}D^{(*)-}$ are thought to be good modes for the observation of CP violation with sensitivity in $sin2\beta$ comparable to the decay $B \to \psi K_s^o$.[3] The branching fractions for these decay modes can be estimated using the measured rates for the analog reactions where the D is replaced with a Cabibbo favored D_s. Making the appropriate substitutions we have:

$$\frac{\mathcal{B} \to D^{(*)+}D^{(*)-}}{\mathcal{B} \to D_s^{(*)+}D_s^{(*)-}} \approx (f_{D^{(*)}}/f_{D_s^{(*)}})^2 tan^2\theta_c \approx \frac{1}{20}(0.9)^2$$

Table 3 gives the expected $B^o \to D^{(*)+}D^{(*)-}$ branching fractions where the CLEO measurements for the D_s modes have been used.[4]

Table 3: $B^o \to D^{(*)+}D^{(*)-}$ branching ratio estimates.

Mode	BR of D_s mode (%)	Estimated BR (%)
$B^o \to D^{*+}D^{*-}$	2.4	0.097
$B^o \to D^{*+}D^- + D^+D^{*-}$	2.0	0.081
$B^o \to D^+D^-$	1.1	0.045

An integrated luminosity of 3.09 fb^{-1} ($3.3 \times 10^6 B\bar{B}$ pairs) taken at the $\Upsilon(4S)$ was used for this analysis. Charged tracks were required to be consistent with originating from a primary vertex in both the $r-\phi$ and $r-z$ planes. Photon candidates were required to have energies greater than 30 MeV if $|cos\theta| < 0.71$ (θ=polar angle) and greater than 50 MeV for other regions of the CsI calorimeter. Pairs of photons with invariant mass within $\pm 2.5\sigma$ of the nominal π^o mass were

kept for further consideration. Both dE/dx and time of flight information were used to distinguish charged kaons from pions.

Candidate D^{*+}'s were reconstructed using the $D^{*+} \to \pi^+ D^o$ mode while D^o's were reconstructed using the modes $D^o \to K^-\pi^+$, $K^-\pi^+\pi^o$, and $K^-\pi^-\pi^+\pi^+$. Only the mode $D^+ \to K^-\pi^+\pi^+$ was used for D^+ candidates. The $D^* - D$ mass resolution for modes containing a D^{*+} decay into all charged tracks was improved by performing a vertex constrained fit.

Backgrounds from non-B sources were minimized using the beam constrained mass and energy difference ($\Delta E = E_B - E_{beam}$). Since the decays under study here are all of the form $Pseudoscalar \to Vector + Pseudoscalar$ a cut of $|cos\theta_{helicity}| > 0.5$ was used in the analysis. Background events are expected to have a flat $|cos\theta_{helicity}|$ distribution.

The results of this analysis are displayed in Fig. 2 where ΔE vs. m_B is plotted for the three decay modes. In each case the signal region is given by the box and the sideband regions lie above and below the dotted lines. Table 4 gives a summary of the event yields and 90% confidence level upper limits for each mode. The probability that the expected background of 0.022±0.011 events in the $B^o \to D^{*+}D^{*-}$ channel fluctuates up to or exceeds the observed one event is ≈2.2%. If we interpret this one event to be a signal then the corresponding branching fraction is:

$$\mathcal{B}(B^o \to D^{*+}D^{*-}) = [6.0^{+8.1}_{-4.2}(stat) \times 10^{-4}] \times [1 \pm 0.18(syst)]$$

where the systematic error is largely due to uncertainties in the D and D^* branching fractions, and tracking efficiencies. No significant excess of events is found in the other two modes.

Table 4: Summary of $B^o \to D^{(*)+}D^{(*)-}$ analysis.

Mode	Evts. in ΔE sidebands	Pred. Bkgd. in signal region	Evts. in signal region	Upper Limit 90% CL
$D^{*+}D^{*-}$	4	0.022±0.11	1	2.5×10^{-3}
$D^{*+}D^- + D^+D^{*-}$	117	0.64±0.10	2	2.0×10^{-3}
D^+D^-	539	2.64±0.34	3	1.3×10^{-3}

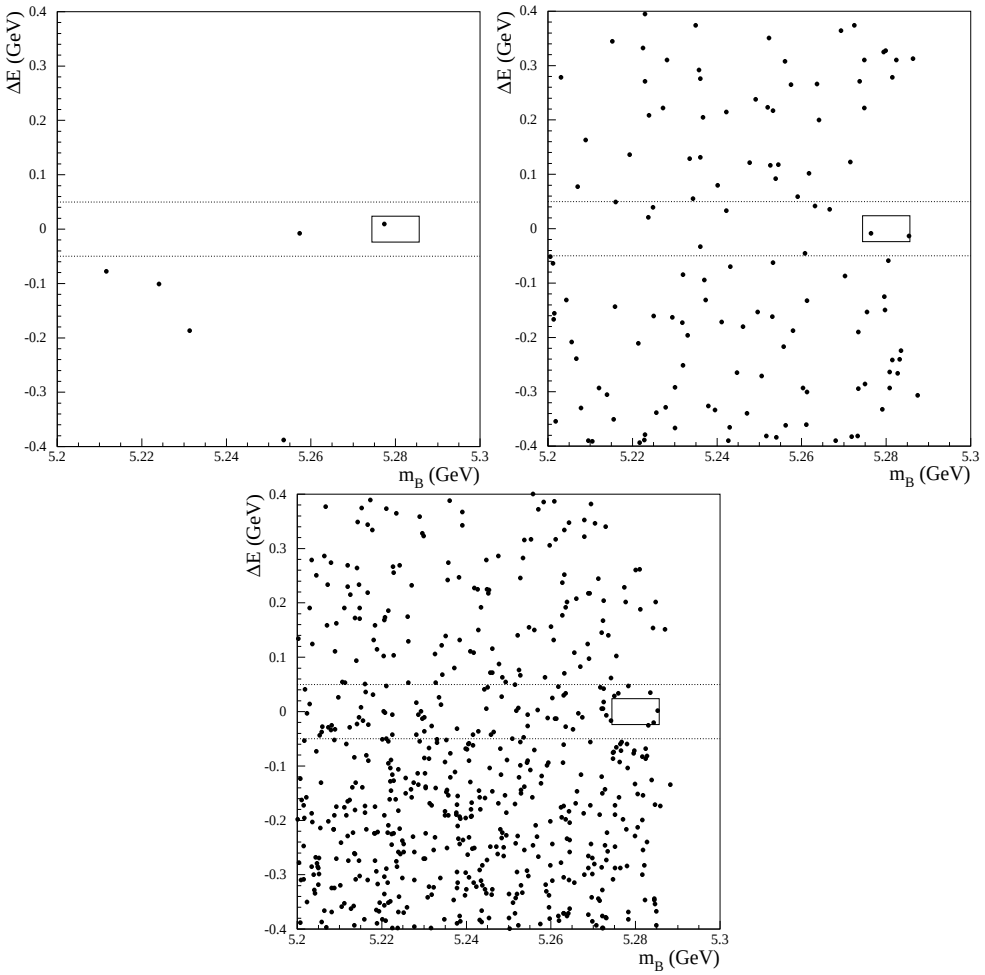

Figure 2: ΔE *vs.* m_B for data. The signal region is indicated by the box. The sideband region lies above and below the dotted lines.

2.2 Non-resonant Three Body Hadronic B-meson Decays

Decays of charged B mesons to three charged hadrons are of interest as they may exhibit CP violation. In particular, decays of the form $B^+ \to h^+h^-h^+$ where h can be a $\pi^\pm, K^\pm, p$ or $\bar{p}$ may have CP asymmetries as large as 10% when the h^+h^- invariant mass is close to the η_c or χ_{co} mass.[5] The non-resonant decay $B^+ \to \pi^+\pi^-\pi^+$ is predicted[6] to have a branching fraction in the range (1.5-8.4)$\times 10^{-5}$. Here the authors point out that interference between the non-resonant amplitude (with $m(\pi^+\pi^-) \approx 3.4$GeV) and $B \to \chi_{co}$, $\chi_{co} \to \pi^+\pi^-$ could lead to a CP asymmetry of (0.4-0.8)$sin\gamma$, with $\gamma = \arg V_{ub}^*$. If this is so, then γ can be measured at an e^+e^- facility operating at the Υ(4S).

The CLEO collaboration has searched for these decays using 3.2 fb^{-1} of data taken at the Υ(4S) and 1.1 fb^{-1} of data taken at energies about 60 MeV below the Υ(4S). The continuum event background (non-$B\bar{B}$ events) is greatly reduced using a combination of event shape cuts and kinematic based criteria optimized for three body B decay. Charged tracks in hadronic events are identified as $\pi^\pm, K^\pm, p$ or $\bar{p}$ using dE/dx information from the central drift chamber system. B-meson related backgrounds (e.g. $B \to \psi K$) are suppressed by vetoing any event where a charged track is identified as either an electron or muon or the invariant mass of oppositely charged tracks is within 60 (40) MeV of the ψ (D^o) mass. The detection efficiency of each mode listed in Table 5 is determined using a GEANT[7] based Monte Carlo simulation. In all cases the energy of the B-meson is constrained to be the same as the beam energy.

The mass distributions for the various decay modes are shown in Fig. 3. The signal region for each mode is shown between the arrows. Unfortunately, there is no signal in any of the mass plots. The details of the analysis are summarized in Table 5 and 90% confidence level upper limits are given in Table 6. While this analysis does not find any evidence for these decay modes it does rule out a substantial range of the predicted branching fraction for $B^+ \to \pi^+\pi^-\pi^+$ and provides improved limits in all other cases.

2.3 Electromagnetic Penguin Decays of the B-meson

The first direct observation of penguin mediated B-meson decay was by CLEO in 1993[11] with the observation of $B \to K^*\gamma$. Precision measurements of this decay rate as well as other other penguin decays give a new window into and perhaps

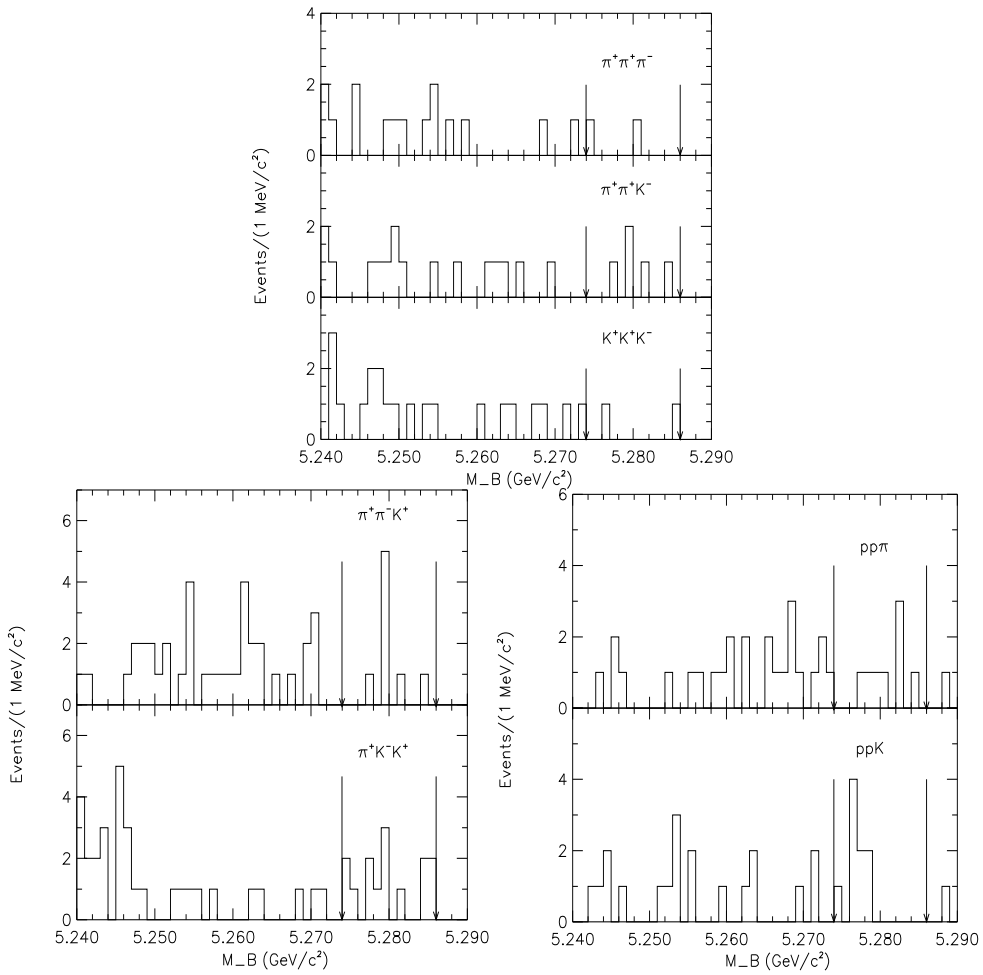

Figure 3: Mass distributions for the various $B^+ \to h^+h^-h^+$ modes. In all cases the signal region is between the arrows

Table 5: Summary of $B^+ \to h^+h^-h^+$ analysis.

Mode	Signal yield	Est. Bkgd.	Efficiency (%)	90 % CL Upper Limit No. Events
$B^+ \to \pi^+\pi^-\pi^+$	2	1.2±1.2	4.5±0.66	5.3
$B^+ \to \pi^+\pi^+K^-$	5	3.9±1.8	4.5±0.66	7.2
$B^+ \to \pi^+\pi^-K^+$	8	13.0±4.0	7.1±1.1	5.6
$B^+ \to \pi^+K^-K^+$	14	8.8±3.0	6.7±0.98	14.3
$B^+ \to K^+K^+K^-$	2	3.9±2.0	3.6±0.54	3.9
$B^+ \to p\bar{p}\pi^+$	8	8.6±2.4	4.8±0.7	7.2
$B^+ \to p\bar{p}K^+$	9	4.3±1.5	4.5±0.66	11.4

beyond the standard model as they involve internal loops with heavy mass quarks and vector bosons (Fig. 4). In addition, the mode $B \to K^*\gamma$ is important as it can be used to constrain the models used to estimate form factors in semi-leptonic $b \to u$ decay, e.g. $B \to \rho l\nu$. The decay $B \to \rho\gamma$ is similar to $B \to K^*\gamma$ but has a decay rate that is dependent on the CKM matrix element $|V_{td}|$ rather than $|V_{ts}|$. Given the difficulty with measuring direct t-quark decays, the simultaneous measurement of $B \to \rho\gamma$ and $B \to K^*\gamma$ offers the best opportunity to determine $|V_{td}|/|V_{td}|$ for the near term future.

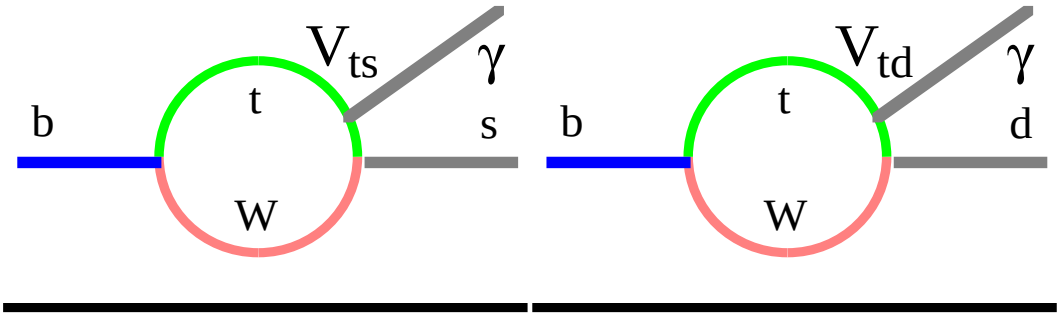

Figure 4: Electromagnetic penguin decay.

The CLEO collaboration has updated its electromagnetic penguin decay analysis by using a larger data set than used in the 1993 analysis. This new analysis uses 2.4 fb^{-1} of data taken at the Υ(4S) and 1.1 fb^{-1} of data taken at energies about 60 MeV below the Υ(4S). Candidate B-mesons are formed by combining a vector meson (ρ, ω, or K^*) with a high energy photon. The mass resolution of a

Table 6: Comparison of branching fractions with previous results and theoretical predictions.

Mode	90 % CL Upper Limit (10^{-5})	Previous best limit (10^{-5})	Prediction (10^{-5})
$B^+ \to \pi^+\pi^-\pi^+$	4.1	5.0[8]	1.5-8.4[6]
$B^+ \to \pi^+\pi^+K^-$	5.6	-	-
$B^+ \to \pi^+\pi^-K^+$	2.8	19[9]	-
$B^+ \to \pi^+K^-K^+$	7.5	-	-
$B^+ \to K^+K^+K^-$	3.8	20[10]	-
$B^+ \to p\bar{p}\pi^+$	5.3	8.4[8]	-
$B^+ \to p\bar{p}K^+$	8.9	-	-

candidate B is improved using the beam energy in place of the measured energies. In Fig. 5 the invariant mass of $B \to K^*\gamma$ candidates for the various K^* modes is shown. Backgrounds to this analysis arise from processes that produce either high energy photons or high energy π^o's and η's that are reconstructed as single showers in the calorimeter. High energy photons are produced by initial state radiation (ISR) while high energy π^o's and η's can be present in non-resonant e^+e^- annihilation events ($Q\bar{Q}$). Extreme care is taken in this analysis to suppress backgrounds from these sources. A combination of event shape cuts (Fox-Wolfram moment R_2, thrust axis) and a Fisher discriminant (Fig. 6) effectively remove contamination from ISR and $Q\bar{Q}$ events.

The $B \to K^*\gamma$ analysis is also subject to contamination from $B \to \rho\gamma$ events where a charged pion is misidentified as a kaon. In order to distinguish between these two types of B decay a neural network is employed. The neural network uses the following inputs: $\Delta E_{\pi\pi}$, $M_{K\pi}$, $M_{\pi\pi}$, and $cos\theta_\rho$. Here θ_ρ is the angle found by transforming the momentum vector of the ρ's daughter with the larger momentum into the ρ's rest frame and measuring the angle between this transformed momentum vector and the flight direction of the ρ in the lab frame. In Fig. 7 the output from the neural network for $B \to K^*\gamma$ (peak at -1) and $B \to \rho\gamma$ (peak at +1) Monte Carlo events is shown.

In Fig. 8 the data is shown for the various K^* decay modes. The box in each figure represents the signal region in the ΔE, M_B plane. A maximum likelihood

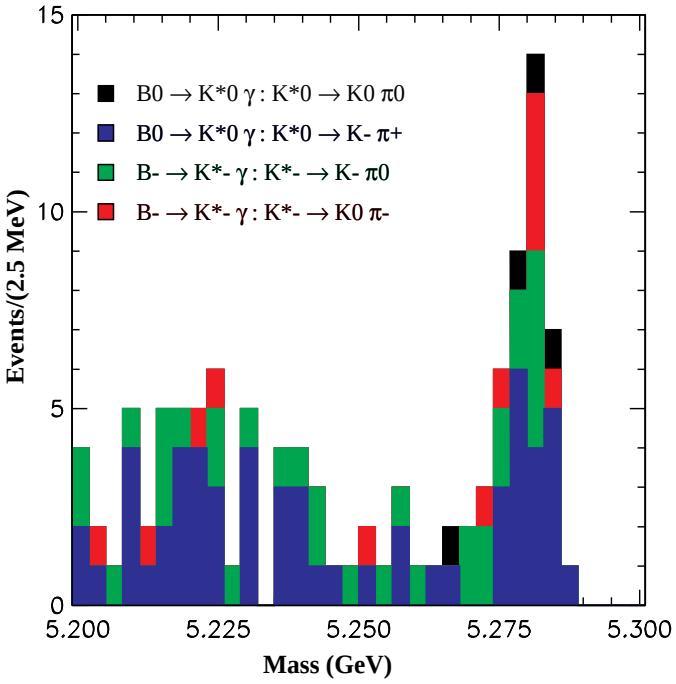

Figure 5: Mass plot for $B \to K^{*}\gamma$ candidates.

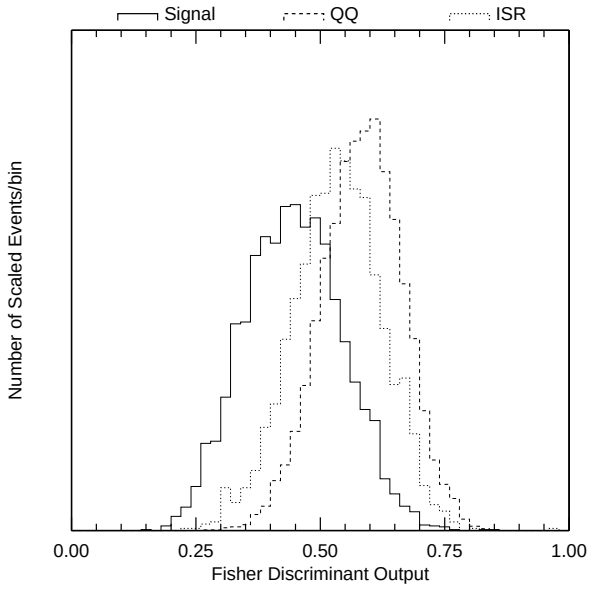

Figure 6: The distribution of the Fisher discriminant output for a Monte Carlo sample of $B^o \to K^{*o}\gamma(K^{*o} \to K^+\pi^-)$ signal, $Q\bar{Q}$, and initial state radiation (ISR) events. The histograms all have equal area.

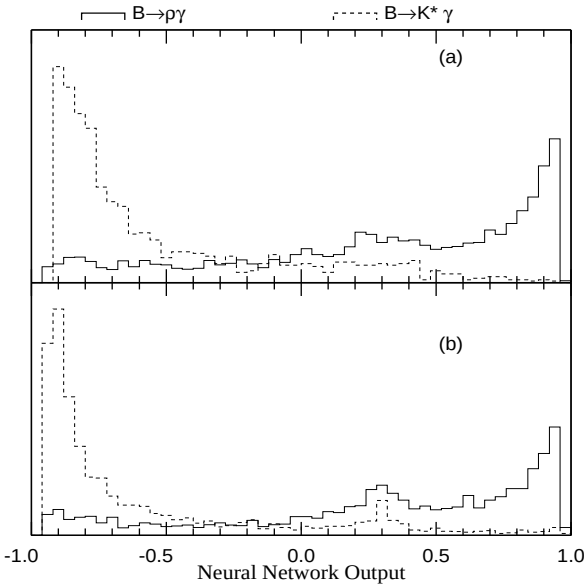

Figure 7: Distribution of the output of the neural network for Monte Carlo samples of (a) $B^o \to \rho^o\gamma$ and $B^o \to K^{*o}\gamma$ ($K^{*o} \to K^+\pi^-$) and (b) $B^- \to \rho^-\gamma$ and $B^- \to k^{*-}\gamma$ ($K^{*-} \to K^-\pi^o$).

fit using M_B, $M_{K\pi}$, ΔE, and the Fisher discriminant is used to determine the signal and background for each K^* mode. Table 7 gives the number of signal events, efficiency, and branching fraction for each K^* mode. The first error on the branching fraction is from the maximum likelihood fit and includes statistical and systematic errors. The second error is due to the uncertainty in the efficiency. In Table 8 the combined $B \to K^*\gamma$ branching fraction is given for both the old and new analysis. The new results are in good agreement with the previous CLEO results.

Table 7: Individual $B \to K^*\gamma$ branching ratios.

K^* Mode	Signal Evts.	Signal Eff. (%)	Branching Ratio (10^{-5})
$K^+\pi^-$	$24.2^{+6.1}_{-5.6}$	22.3±2.0	$4.2^{+1.1}_{-1.0} \pm 0.4$
$K^o\pi^o$	$2.8^{+2.0}_{-1.5}$	1.8±0.2	$6.1^{+4.2}_{-3.3} \pm 0.8$
$K^o\pi^-$	$6.3^{+3.0}_{-2.5}$	5.7±0.6	$4.3^{+2.1}_{-1.7} \pm 0.5$
$K^-\pi^o$	$4.6^{+4.4}_{-3.0}$	6.9±0.7	$2.6^{+2.5}_{-1.7} \pm 0.3$

Table 8: Comparison of old and new $B \to K^*\gamma$ branching ratios.

Mode	New Branching Ratio (10^{-5})	Old Branching Ratio (10^{-5})
$B^o \to K^{*o}\gamma$	$4.4\pm1.0 \pm 0.6$	$4.0\pm1.7 \pm 0.8$
$B^- \to K^{*-}\gamma$	$3.8^{+2.0}_{-1.7} \pm 0.5$	$5.7\pm3.1 \pm 1.1$
$B \to K^*\gamma$	$4.2\pm0.8 \pm 0.6$	$4.5\pm1.5 \pm 0.9$

There are many predictions[12] for the ratio $\mathcal{B}(B \to K^*\gamma)/\mathcal{B}(B \to s\gamma)$ as shown in Fig. 9. By combining CLEO's previous measurement[13] of

$$\mathcal{B}(B \to s\gamma) = (2.32 \pm 0.57 \pm 0.35) \times 10^{-4}$$

with these new results we obtain:

$$\frac{\mathcal{B}(B \to K^*\gamma)}{\mathcal{B}(B \to s\gamma)} = 0.181 \pm 0.068.$$

This result is shown in Fig. 9 along with a number of theoretical predictions for this ratio. Clearly, more precise measurements and calculations are needed to discriminate between the models.

The $B \to (\rho\omega)\gamma$ analysis suffers from a lack of statistics in comparison to the $B \to K^*\gamma$ analysis. Since the candidate sample is so small, signals (or limits) are extracted by cutting on variables rather than performing a maximum likelihood analysis. In Fig. 10 events which pass all cuts are plotted in the M_B, ΔE plane. The events within the signal region (rectangle in Fig. 10) as well the various background estimates are given in Table 9. There is no signal apparent in the $B \to \rho^-\gamma$ and $B \to \omega\gamma$ channels. While there are four events in the signal region for $B \to \rho^o\gamma$ these events all have low values of ΔE and neural net output values marginally consistent with that expected from true $B \to \rho^o\gamma$ events. Hence these four events are not to be taken as evidence for $B \to \rho^o\gamma$. The 90% upper limit confidence levels for these decay modes are given in Table 10. The upper limit for $B \to \rho^-\gamma$ is still about an order of magnitude higher than the theoretical estimates from Soares[14] ((0.04-0.07)$\times 10^{-5}$) and Greub *et al.*[15] ((0.12-0.30)$\times 10^{-5}$).

The ratio of rates for $B \to K^*\gamma$ and $B \to (\rho\omega)\gamma$ can be related to the CKM matrix elements $|V_{ts}|$ and $|V_{td}|$ through:

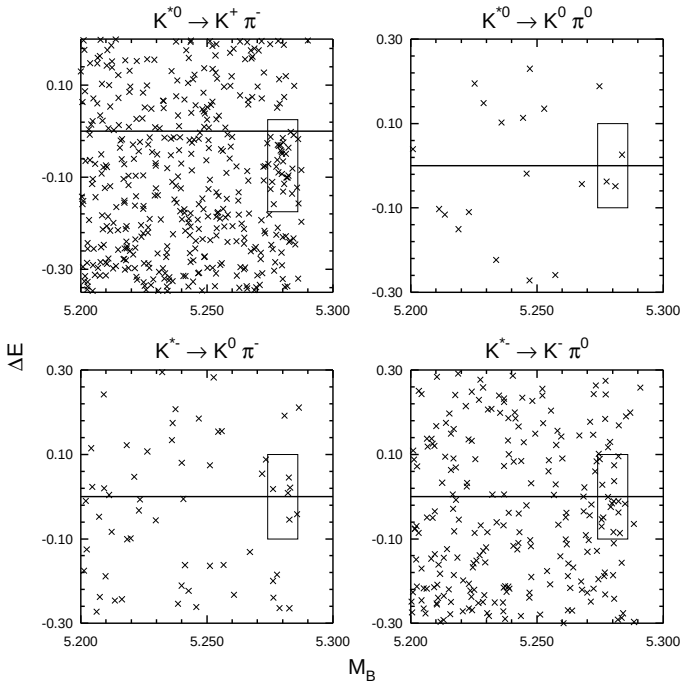

Figure 8: Distribution of $B \to K^*\gamma$ events in the M_B and ΔE plane.

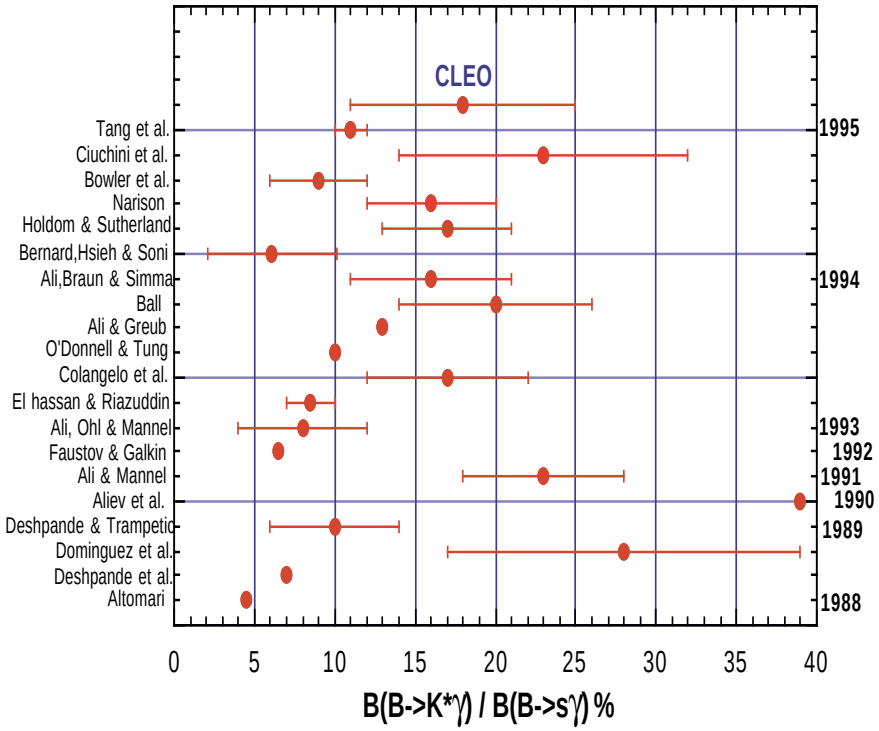

Figure 9: Summary of $\frac{\mathcal{B}(B\to K^*\gamma)}{\mathcal{B}(B\to s\gamma)}$ predictions and the CLEO result.

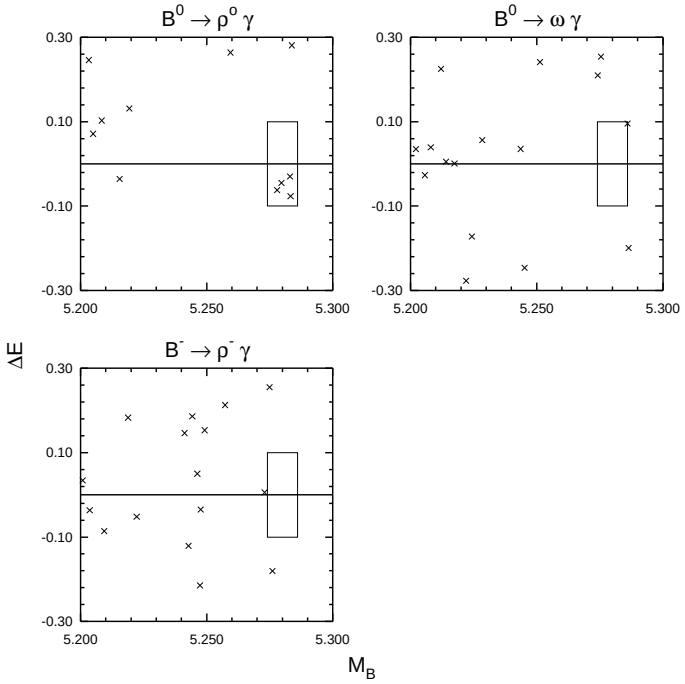

Figure 10: Distribution of $B \to (\rho\omega)\gamma$ events in the M_B and ΔE plane.

$$\frac{\mathcal{B}(B^- \to \rho^-\gamma)}{\mathcal{B}(B^- \to K^{*-}\gamma)} = \frac{\mathcal{B}(B^o \to \rho^o\gamma) + \mathcal{B}(B^o \to \omega\gamma)}{\mathcal{B}(B^o \to K^{*o}\gamma)} = |\frac{V_{td}}{V_{ts}}|^2 \Omega\xi.$$

Here we neglect contributions from long distance effects. In the above equation ξ accounts for $SU(3)$ symmetry breaking and Ω accounts for the difference in phase space. An upper limit combining all the modes can be calculated if one assumes that $\mathcal{B}(B \to K^{*o}\gamma) = \mathcal{B}(B \to K^{*-}\gamma)$. Doing so we obtain:

Table 9: Events and background estimates.

	$B \to \rho^o\gamma$	$B \to \omega\gamma$	$B \to \rho^-\gamma$
Events	4	0	0
QQ	0.23±0.08	0.56±0.18	0.40±0.11
ISR	0.18±0.12	0.14±0.10	0.12±0.09
$B \to K^*\gamma$	0.45±0.11	0.0	0.27±0.06
SUM	0.85±0.17	0.70±0.14	0.79±0.14

Table 10: Branching fraction upper limits @ 90% C.L.

Mode	Signal events	Eff. (%)	Branching Fraction (10^{-5})
$B \to \rho^o\gamma$	4(7.99)	9.2±1.3	< 3.9
$B \to \omega\gamma$	0(2.30)	8.9±1.2	< 1.3
$B \to \rho^-\gamma$	0(2.30)	9.2±1.3	< 1.1

$$\frac{\mathcal{B}(B \to (\rho\omega)\gamma)}{\mathcal{B}(B \to K^*\gamma)} < 0.19.$$

The phase space factor Ω can be estimated using[16]:

$$\Omega = \frac{(m_b^2 + m_d^2)}{(m_b^2 + m_s^2)} \frac{(m_B^2 + m_\rho^2)^3}{(m_B^2 + m_{K^*}^2)^3}.$$

Assuming m_b =5 GeV, m_s=300 MeV, m_d=100 MeV and the nominal masses for m_B, m_{K^*}, and m_ρ we obtain $\Omega = 1.02 \pm 0.02$. The SU(3) term ξ has been evaluated by several groups. In Table 11 estimates of ξ as well as the upper limits on the ratio $|V_{td}|/|V_{ts}|$ are given. These limits are comparable to recent ALEPH results[18] which rely on B_s^o oscillations.

Table 11: Upper limits for $|V_{td}|/|V_{ts}|$.

Group	Model	ξ	Upper Limit
Ali,*et al.*[16]	QCD Sum Rule	0.58	< 0.56
Soares[14]	BSW Formalism	0.72-0.90	$< (0.45 - 50)$
Narison[17]	Hybrid QCD Sum Rule	0.77	< 0.49

2.4 Search for $b \to s$ Gluonic Penguins using inclusive η' and K^o_s Decays

To date there is no experimental evidence for gluonic penguin decay in the b-quark sector. Unlike the photon radiated in an electromagnetic penguin decay the gluon is not directly observable in the CLEO detector. This greatly complicates the search strategy for these decays. One way to look for gluonic penguin decay

is to take advantage of the kinematics of the underlying $b \to sg$ reaction and search for events in a phase space region forbidden to $b \to c$ decays. For example $b \to sg \to s\bar{s}s$ can hadronize into $B \to \eta\prime X_s$ (X_s a meson system containing a strange quark) and produce an $\eta\prime$ with momentum larger than that possible from the analog charm reaction $B \to \eta\prime X_c$. Another such example is $b \to sg \to s\bar{d}d$ which can hadronize to $B \to K_s X$ (X a meson containing no strange quarks), the K_s produced with momentum greater than that possible from $B \to K_s X_c$.

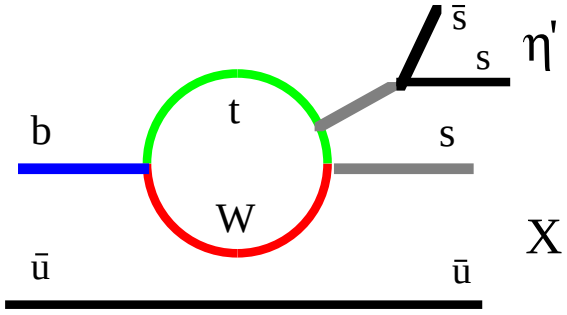

Figure 11: Penguin decay of $b \to \eta\prime X$.

Inclusive searches for $b \to sg$ have two possible advantages over exclusive searches. First, the rate for inclusive $b \to sg$ can be reliably calculated and is not subject to the same uncertainties as the exclusive calculations. Second, the rate for inclusive $b \to sg \to sq\bar{q}$ (with $q = u, d, s$) is expected to be of order 1%[19,20] with $b \to s\bar{s}s$ expected to be $\approx 0.2\%$.[20] This is in contrast to two body exclusive modes such as $\bar{B}^o \to \phi K_s$ or $\bar{B}^o \to K^-\pi^+$ which have rates estimated to be in the 10^{-5} range.

The signature for a $B \to \eta\prime X_s$ gluonic penguin decay is an $\eta\prime$ with $2.0 < p_{\eta\prime} < 2.7$ GeV/c. This kinematic region eliminates most of the $\eta\prime$'s produced by $b \to c$ transitions. Backgrounds from $b \to c$ transitions (e.g. $B \to D^{(*)o}\eta\prime$) can only contribute to the region $2.0 < p_{\eta\prime} < 2.34$ GeV/c.

There are many sources of K_s's in B decay including $B \to D_s X$, $B \to D^o X$, $B \to D^+ X$, and $B \to \Lambda_c X$. However, these sources produce K_s's with $p_{K_s} < 2$ GeV/c. Thus a signature for $b \to sg$ is an excess of K_s's produced in B decay with $p_{K_s} > 2$ GeV/c. The most important background in this momentum region is from the Cabibbo suppressed internal spectator decay $B \to K_s D^{(*)}$.

The data sample used in this analysis consists of 3.1 fb^{-1} ($3.3 \times 10^6 B\bar{B}$ pairs) of data taken at the Υ(4S) and 1.6 fb^{-1} of data taken at energies below the Υ(4S).

Hadronic continuum events are suppressed using a combination of event shape cuts and a Fisher discriminant. To reconstruct an $\eta\prime$ first the η is reconstructed through the $\eta \to \gamma\gamma$ mode and then the η is combined with pairs of oppositely charged pions. The K_s decays are reconstructed through the $K_s \to \pi^+\pi^-$ mode. For convenience the analysis is done using the scaled momentum of the meson $(\eta\prime, K_s)$:

$$x = \frac{p_{meson}}{\sqrt{E^2_{beam} - m^2_{meson}}}$$

to aid in the continuum subtraction. In terms of x the region $0.45 < x_{\eta\prime} < 0.52$ is heavily populated by $b \to sg \to \eta\prime X_s$ while for $b \to sg \to K_s X$ the interesting region is $0.46 < x_{K_s} < 0.54$.

In Fig. 12 the inclusive continuum subtracted x spectrum of K_s's and $\eta\prime$'s from B-meson decay is shown. There is no apparent $b \to sg$ signal in the K_s x spectrum. The data can be used to calculate 90% upper limit confidence levels of:

$$\mathcal{B}(B \to K_s X) < 7.5 \times 10^{-4}$$

for $0.40 < x_{K_s} < 0.54$ and

$$\mathcal{B}(B \to K_s X) < 2.1 \times 10^{-4}$$

for $0.46 < x_{K_s} < 0.54$.

For $B \to \eta\prime X$ there is a modest excess ($\approx 2\sigma$) of $\eta\prime$'s in the region of interest. However, this is not compelling evidence for $b \to sg$ at this time, so we quote 90% upper limit confidence levels of:

$$\mathcal{B}(B \to \eta\prime X) < 7.4 \times 10^{-4}$$

for $0.45 < x_{\eta\prime} < 0.52$ and

$$\mathcal{B}(B \to \eta\prime X) < 17 \times 10^{-4}$$

for $0.39 < x_{\eta\prime} < 0.52$.

2.5 Search for $B^+ \to \omega h^+$ and $B^+ \to \eta h^+$

Two body decays of B-mesons into final states containing either an ω or η and a charged pion or kaon are sensitive probes of the standard model as they can be described by either hadronic penguin or spectator $b \to u$ graphs. For example,

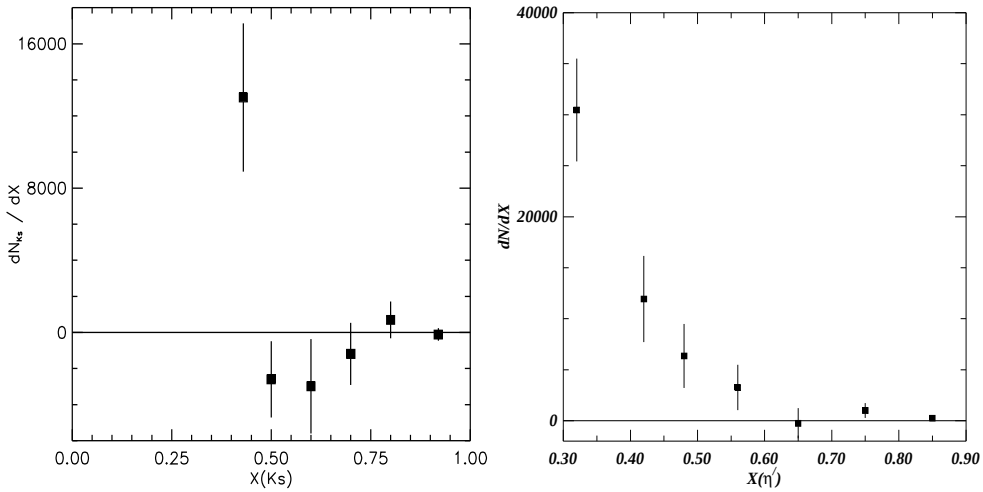

Figure 12: The continuum subtracted yield of K_s's and $\eta\prime$'s as a function of the scaled momentum x.

as shown in Fig. 13 $B^+ \to \omega\pi^+$ can occur as the result of a spectator $b \to u$ decay while $B^+ \to \omega K^+$ can result from gluonic penguin decay. Theoretical predictions[21] for these decays range from 3×10^{-7} to 1.1×10^{-5} while previous experimental upper limits are in the 10^{-4} range.[1]

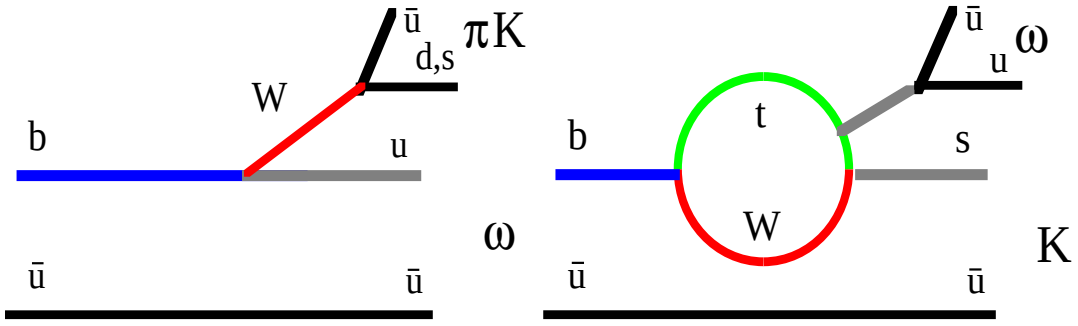

Figure 13: $B^- \to \omega h^-$ via spectator and penguin graphs.

The data used in this analysis consist of 3.1 fb^{-1} ($3.3 \times 10^6 B\bar{B}$ pairs) taken at the $\Upsilon(4S)$ and 1.6 fb^{-1} of data taken at energies slightly below the $\Upsilon(4S)$. As in many other CLEO analyses, continuum suppression is achieved by a combination of event shape cuts and use of a Fisher discriminant. Both the η's and ω's were reconstructed using the $\pi^+\pi^-\pi^o$ decay mode. Charged pion candidates were required to have drift chamber dE/dx within 3σ of their expected value. However, no particle identification cuts were applied to the h^+ in these decays. Candidates for $B^+ \to \omega h^+$ and $B^+ \to \eta h^+$ were formed by combining reconstructed η's and

ω's with a charged track. Here the beam energy and known B mass was substituted for the measured quantities. The events passing all selection criteria are shown in Fig. 14. In these figures the signal region is the area inside the box.

The results of this analysis are presented in Table 12. There are no $B \to \eta h^+$ candidates which leads to a 90% confidence level upper limit on the branching fraction of $< 3.0 \times 10^{-5}$. There are ten events in the signal region for $B \to \omega h^+$ with a predicted background of only 2 events. Assuming binomial statistics, the probability of the observed signal to be a background fluctuation is only 1.2×10^{-4}. This observed excess over the background corresponds to a branching fraction of $(2.8 \pm 1.0 \pm 0.5) \times 10^{-5}$ where the first error is due to statistics and the second is due to systematics. A more detailed analysis using particle identification to extract the individual branching fractions for $B^+ \to \omega K^+$ and $B^+ \to \omega \pi^+$ is currently in progress.

Table 12: Results for $B^+ \to \omega h^+$ and $B \to \eta h^+$.

Mode	Background	Eff. (%)	Events	Branching Ratio(10^{-5})
ωh^+	2.0±0.3	8.5±1.6	10	2.8±1.0 ± 0.5
ηh^+	0.7±0.2	2.8±0.5	0	<3.0(90% C.L.)

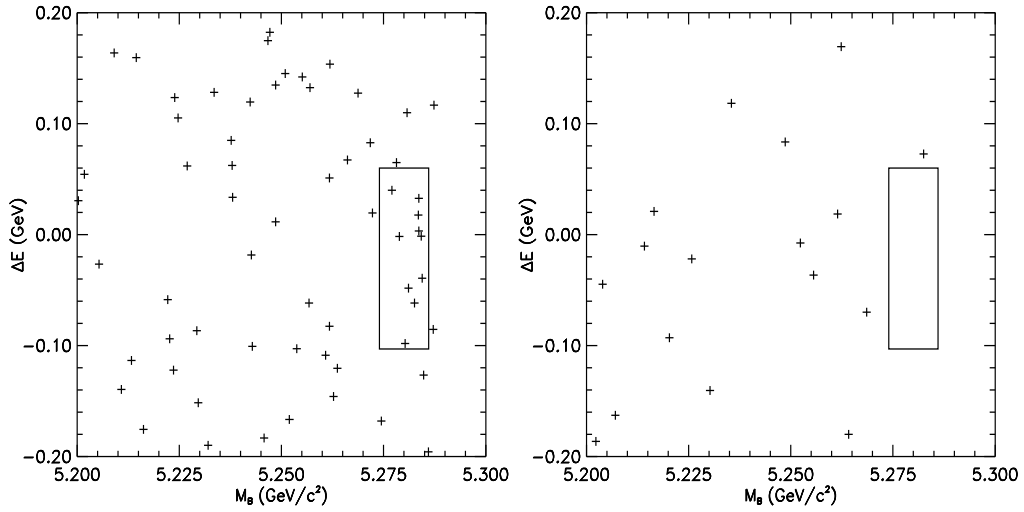

Figure 14: Candidate events for $B^+ \to \omega h^+$ (left) and $B^+ \to \eta h^+$ (right). The boxes indicate the signal regions.

2.6 Measurement of $|V_{ub}|$ using exclusive B-meson Decays

In order to determine the origin of CP violation it is important to measure as precisely as possible the elements of the CKM matrix. The matrix element $|V_{ub}|$ plays in important role in the search for CP violation in the b-quark sector. That $|V_{ub}|$ is not zero was demonstrated first by CLEO[22] and shortly thereafter by ARGUS.[23] Both experiments found evidence for $b \to u$ transitions by studying the lepton momentum spectrum above the $b \to c$ kinematic endpoint. While this method is fine for demonstrating a non-zero value for $|V_{ub}|$ theoretical uncertainties in the lepton momentum spectrum prevent a precise determination of $|V_{ub}|$ with this technique. CLEO has recently side stepped this problem by explicitly reconstructing several semileptonic $b \to u$ decay modes including $B \to \pi l\nu$, $B \to \rho l\nu$, and $B \to \omega l\nu$.

The data used in this analysis consist of 2.66 fb^{-1} ($2.84 \times 10^6 B\bar{B}$ pairs) taken at the Υ(4S). The hermiticity of CLEO is exploited to select Υ(4S) decays where only a single neutrino goes undetected. Here the neutrino energy and momentum is given by $E_\nu = 2E_{beam} - \sum E_i$ and $\vec{p}_\nu = -\sum \vec{p}_i$ respectively. B-mesons decaying via the modes listed above should also satisfy the following constraints, $\Delta E \equiv (E_\nu + E_l + E_m) - E_{beam} = 0$ and $M_{ml\nu} = [E^2_{beam} - (\vec{p}_\nu + \vec{p}_l + \vec{p}_m)^2]^{1/2} = M_B$ where $m = \pi, \rho, \omega$. From Monte Carlo studies (Fig. 15) the resolution in $\vec{p}_\nu$ is determined to be 110 MeV/c.

Electrons are identified by combining drift chamber dE/dx, time of flight, and calorimeter information. Muons are identified by their ability to penetrate the magnet iron. Pairs of photons which have invariant masses within $\pm 2\sigma$ of the π^o mass are kept for further study and are used in decay modes with ρ's and ω's in the final state.

Care must be taken to reduce background without losing too much of the signal. A ten-fold reduction in continuum related backgrounds is achieved using the thrust axis of the ml pair. Additional background reduction is achieved by using only high momentum leptons ($p_l > 1.5$ GeV for π modes and $p_l > 2$ GeV for ρ,ω modes) to discriminate against $b \to c \to\ sl\nu$ decays and to some extent $b \to cl\nu$ decays. Finally, non-$B\bar{B}$ contributions were determined using data taken at energies below the Υ(4S).

In order to extract the decay rate for each mode the data was binned into 11 regions in the $M_{ml\nu}$, ΔE ($5.1075 \leq M_{ml\nu} < 5.2875$ GeV, $|\Delta E| < 75$ MeV) plane.

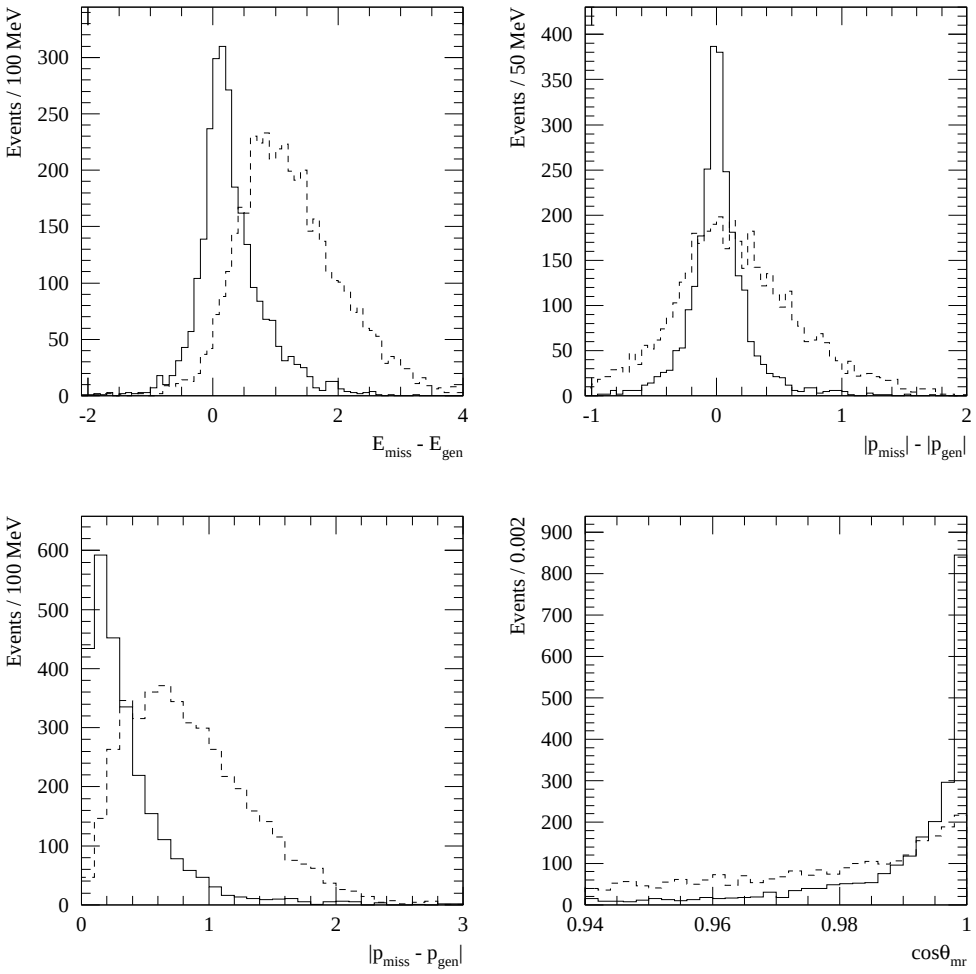

Figure 15: The resolution of neutrino energy, momentum, and angle from $B^o \to \pi^- l^+ \nu$ Monte Carlo events. The solid histograms are distributions when no K_L^o and/or extra neutrinos are present in the event. The dashed histograms had at least one K_L^o and/or extra neutrinos in the event.

For the $\rho l\nu$ ($\omega l\nu$) modes the yield was further subdivided into 4 (5) bins over the 2π (3π) mass range. For all decay modes Monte Carlo simulations were used to provide signal, $b \to c$ backgrounds, cross feed and feed down from higher mass $B \to ul\nu$ states. The isospin and quark symmetry relations $\Gamma(B^o \to \pi^- l^+ \nu) = 2\Gamma(B^+ \to \pi^o l^+ \nu)$ and $\Gamma(B^o \to \rho^- l^+ \nu) = 2\Gamma(B^+ \to \rho^o l^+ \nu) \approx 2\Gamma(B^+ \to \omega l^+ \nu)$ are used to constrain the B^+ rates relative to B^o. Prior to fitting, the data was corrected for backgrounds due to residual continuum and sources of fake leptons. In Fig. 16 the data along with the various background estimates is shown separately for the $B \to \pi l\nu$ and $B \to (\rho, \omega) l\nu$ modes. Here the ISGWII[24] model is used for the normalization. A clear signal over the background is present in both plots. A summary of the data yields for the ISGWII fit is given in Table 13. There

Table 13: Summary of event yields using the ISGWII model.

Yield	$\pi^\pm$	π^o	$\rho^\pm$	ρ^o	ω
Raw	46	19	47	73	7
Corrected	26.6	8.6	19.5	15.1	3.5
Eff.$\times 10^{-2}$	2.3	1.5	1.5	2.4	0.6

are many models of semi-leptonic $b \to u$ decay.[24–28] For each of these models a simultaneous fit for the number of $B \to \pi l\nu$ events (N_π) and $B \to \rho l\nu$ events (N_ρ) is performed. In Fig. 17 the results of such fits are shown. The KS[26] model gives a poor fit to the data (confidence level $< 0.5\%$) while the other models give acceptable fits. Results from these fits are used to calculate the branching fractions shown in Fig. 18. Values for $|V_{ub}|$ are calculated for each model assuming $\tau_{B^o} = 1.56 \pm 0.05$ ps and $\tau_{B^o}/\tau_{B^+} = 1.02 \pm 0.04$. Averaging over the models a value of $|V_{ub}| = (3.3 \pm 0.2^{+0.3}_{-0.4} \pm 0.7) \times 10^{-3}$ is obtained where the uncertainties are statistical, systematic, and model dependence. This value of $|V_{ub}|$ is in good agreement with the previous results using the endpoint of the lepton spectrum.

3 τ Lepton Physics

The CLEO detector is also well suited for the study of τ decay. Its fine grained electromagnetic calorimeter reconstructs π^o's and η's with high efficiency and low background. This combined with excellent charged particle tracking and particle

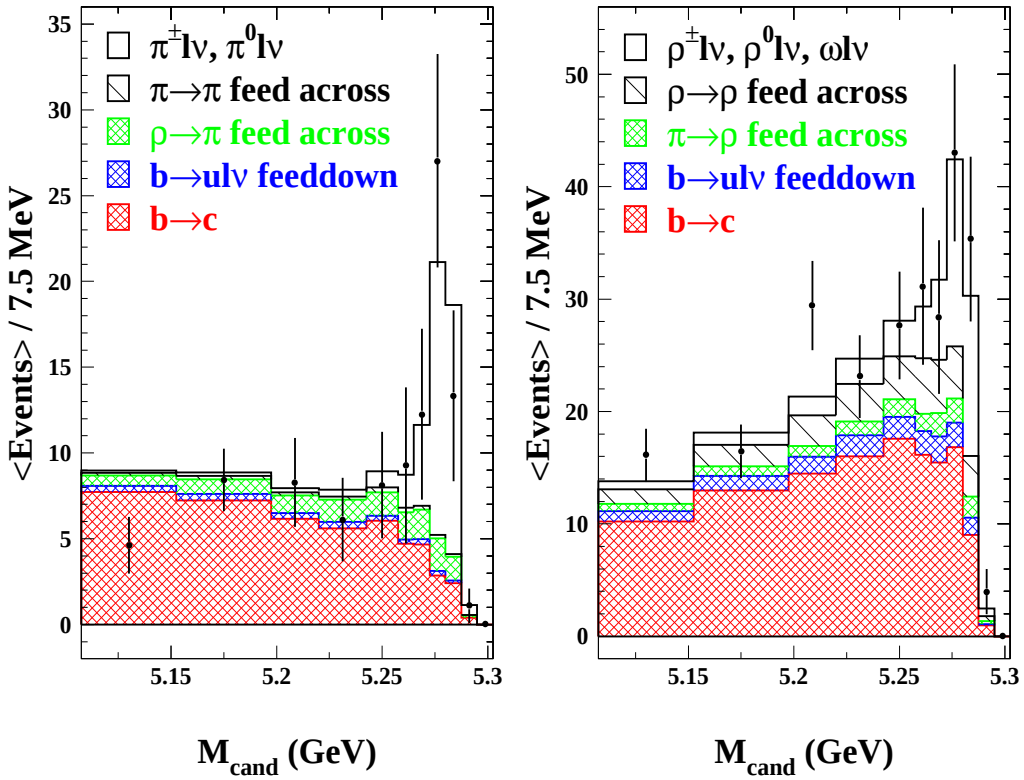

Figure 16: The M_{cand} mass distribution in the ΔE signal band for the combined π and vector meson modes. The data points have been corrected for continuum and background fakes. The ISGWII model is used for normalization.

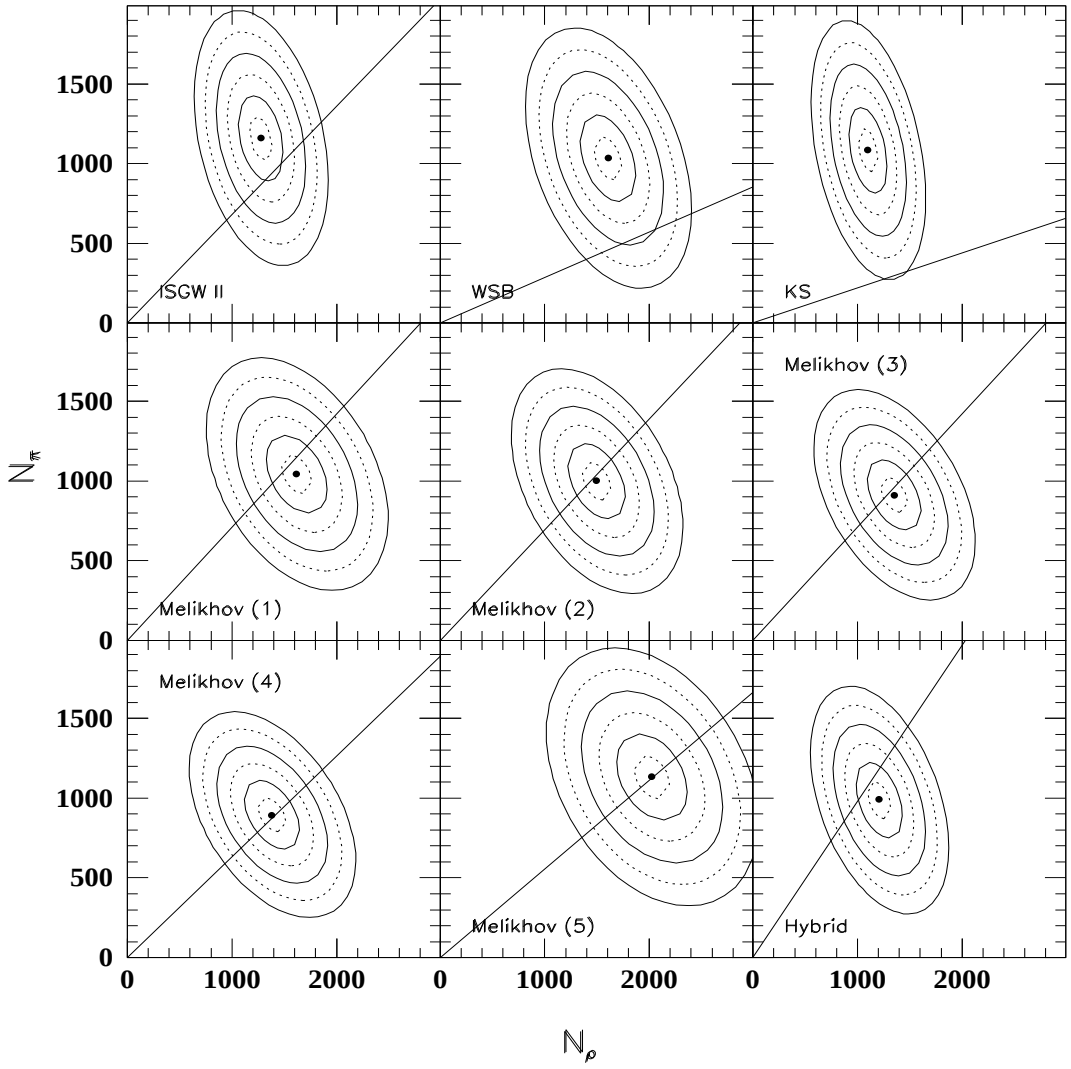

Figure 17: The half sigma contours in the fit parameters N_π vs. N_ρ for the various models. The lines are the ρ/π rates predicted by each model.

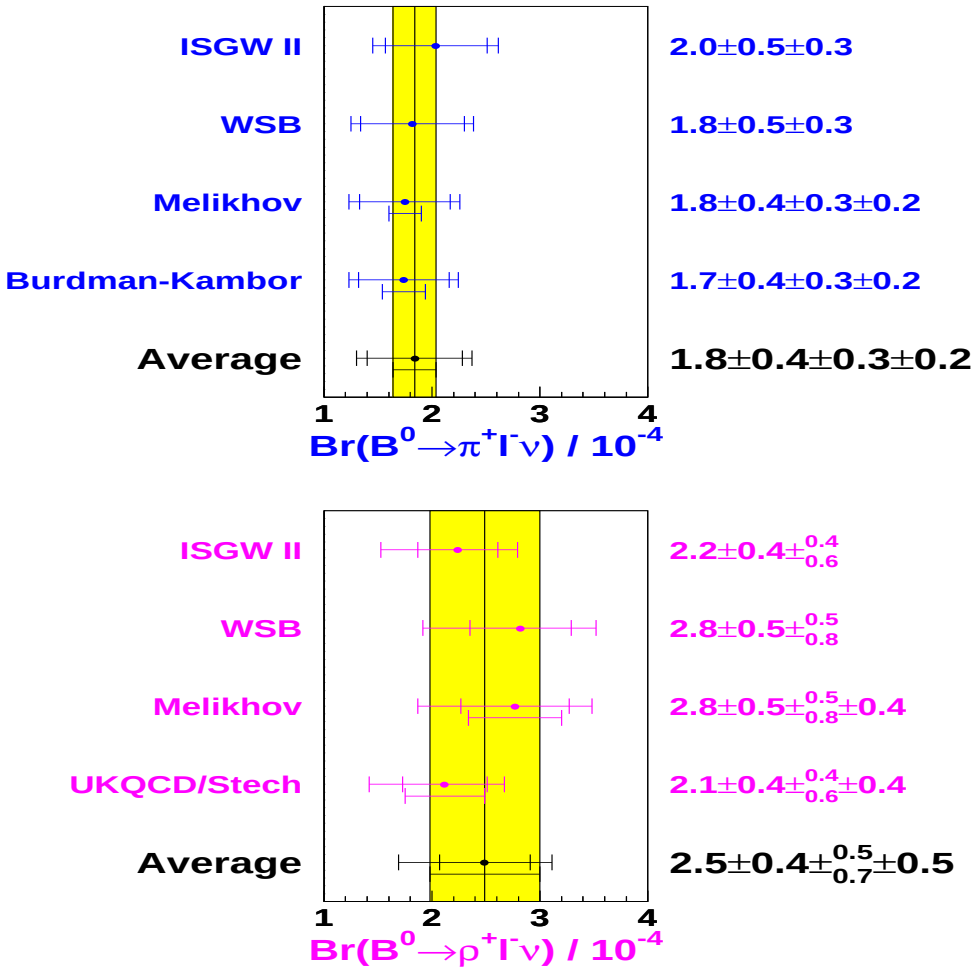

Figure 18: The results for the branching ratios for several models. The central vertical line is the average of the models.

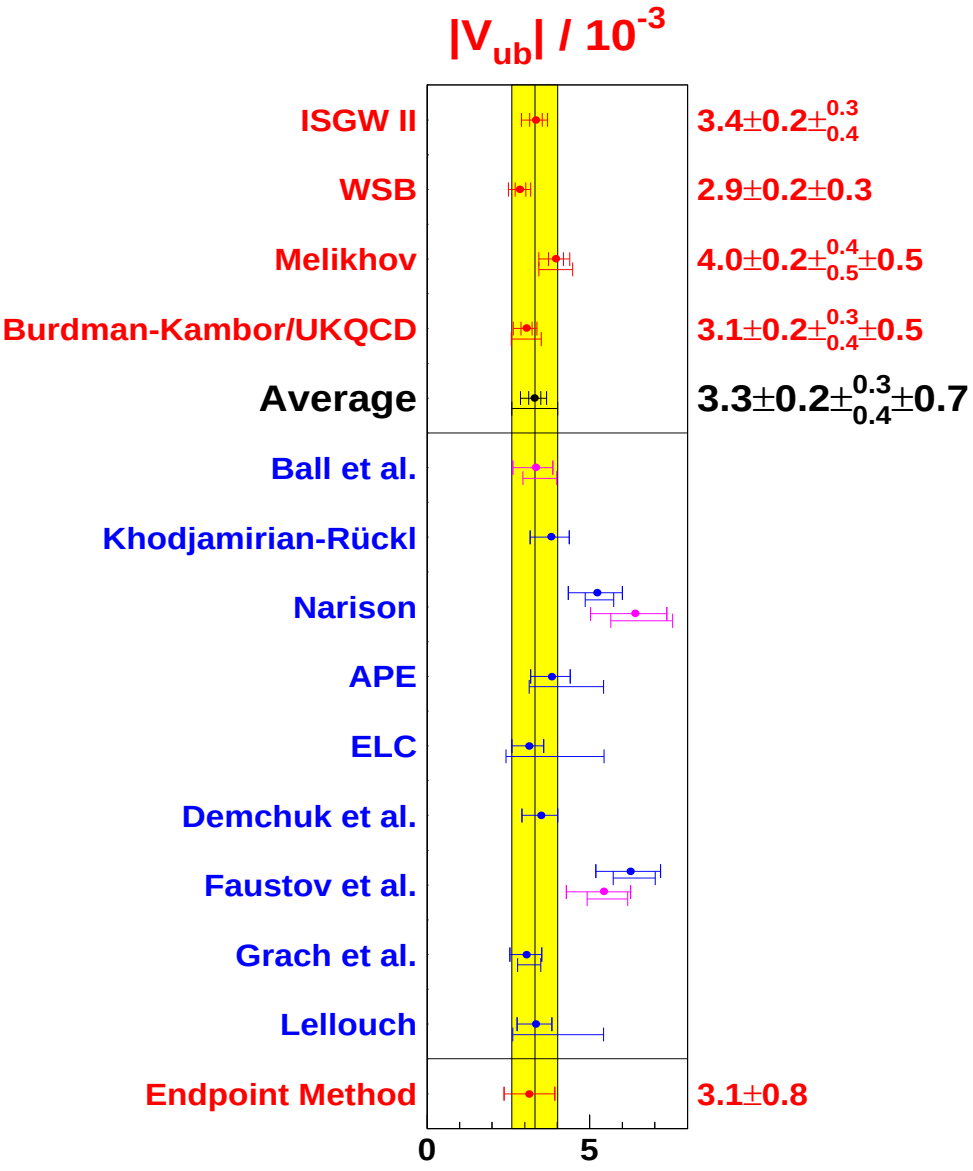

Figure 19: The values of $|V_{ub}|$ from several models of $B \to \pi l\nu$ and $B \to \rho l\nu$ decay. Also included is the value of $|V_{ub}|$ from the lepton endpoint technique. The vertical line is the average of the top four models.

identification (e, μ, π, K^+, K^o, p) over a large momentum range allows for many detailed studies of τ final states.

At the center of mass energies available to CLEO τ leptons are produced through the reaction $e^+e^- \to \tau^+\tau^-$. The cross section for this reaction is "large", approximately 1 nb. To date CLEO has accumulated $\approx 10^7$ τ decays, by far the world's largest data sample. If we neglect intial and final state radiation then each τ is produced with energy equal to the beam energy. Thus like the situation with B-mesons the τ's energy and momentum is a priori accurately known.

Even at CLEO's center of mass energy the τ event topology is jet-like. In addition, a τ event has four or fewer charged tracks $\approx 98\%$ of the time. These two characteristics make it easy to separate $\tau^+\tau^-$ events from $B\bar{B}$ events. A more serious background comes from low multiplicity hadronic events produced via $e^+e^- \to q\bar{q}$ (continuum events). However, with a judicious choice of total energy and momentum cuts and particle identification even the continuum hadronic background can be kept below 1%. The CLEO experiment is therefore in the enviable position of having a high statistics low background sample of τ's to work with. This has allowed CLEO to become the first experiment to perform detailed studies of τ decays with branching fractions in the $10^{-4} - 10^{-5}$ range and search for decay modes with branching fractions $\mathcal{O}(10^{-6})$.

3.1 τ Decays with an η in the Final State

Decays of the τ with an η in the final state are of interest as they provide both valuable information concerning the behavior and violation of several hadronic symmetries and a new system for the study of the weak hadronic current. There is very little information available on these final states due to their small branching fractions. In fact, the Particle Data Group[1] only lists exclusive branching fractions for $\mathcal{B}(\tau^- \to \eta\pi^-\pi^o\nu)$ ($(0.17\pm0.2 \pm 0.2)\%$[29]) and $\mathcal{B}(\tau \to \eta K^-\nu)$ ($(0.026\pm0.02 \pm 0.02)\%$[30]). Other $\tau \to \eta$ modes are expected to be severely suppressed by the chiral anomaly term and phase space.

The CLEO experiment has recently measured the branching fraction of the decay $\tau^- \to \eta h^- h^+ h^- \nu$ at a rate two orders of magnitude larger than predicted.[31] The analysis uses $4.86 fb^{-1}$ (4.27×10^6 τ pairs) of data collected at energies at and slightly below the $\Upsilon(4S)$. Events that are consistent with the 1 vs. 3 topology are searched for η's decaying via $\eta \to \gamma\gamma$ and $\eta \to 3\pi^o$. In Fig. 20 there are clear η

Table 14: CLEO results for $\tau^- \to h^- h^+ h^- \eta \nu$

mode	tags	events	backgd.	BR$\times 10^{-4}$
$\eta \to \gamma\gamma$	$e, \mu, h/\rho$	65.1$\pm$12.9	5.0$\pm$1.1	3.8$\pm$0.8
$\eta \to 3\pi^o$	e, μ	11.2$\pm$3.7	-	5.1$\pm$1.7

signals in both decay modes.

Care must be taken to insure that these events with η's are from τ's and not hadronic in origin. Therefore the η signal is studied as a function of the 1-prong tag as shown in Table 14. Backgrounds from τ events feeding into this decay mode are estimated using Monte Carlo simulations based on the KORALB[32] and TAUOLA[33] computer routines. The CLEO experiment is modeled using the GEANT[7] package. The contribution to the sample from hadronic and 2-photon events is estimated using data rather than Monte Carlo. As listed in Table 14 there is small contamination in the $\eta \to \gamma\gamma$ sample (from hadronic events) and negligible background in the $3\pi^o$ sample. The detection efficiencies are calculated separately for each 1-prong tag and η branching mode. The branching fractions for the two η decay modes are listed in Table 14. Since these results are statistically independent we can average them and find:

$$\mathcal{B}(\tau^- \to \eta h^- h^+ h^- \nu) = (4.1 \pm 0.7 \pm 0.7) \times 10^{-4}.$$

The second error above is the systematic uncertainty in the branching fraction. It includes contributions from background modeling, π^o and η reconstruction, spectral functions, tracking, luminosity, and cross sections. It is interesting to note that this measurement is $\approx 100\times$ larger than the prediction from Pich[31]!

An effort is underway to look for resonant substructure in these $\tau^- \to \eta h^- h^+ h^- \nu$ events. In Fig 21 (left) the $\eta\pi^+\pi^-$ mass is plotted (two entries per event) for the $\eta \to \gamma\gamma$ events. There is an enhancement at the mass of the $f_1(1285)$. In the lower part of Fig 21 (left) a scatterplot of $m_{\eta\pi^+\pi^-}$ vs. $m_{\eta\pi^\pm}$ is presented (four entries per event). This plot suggests that the η is produced through an intermediate state, $a_o(980)$, and the overall decay chain is: $\tau^- \to f_1(1285)\pi^-\nu$, $f_1(1285) \to a_o^+(980)\pi^-$, $a_o^+(980) \to \eta\pi^+$. A fit to the data yields 30.4$\pm$8.8 events. To convert these events into a branching fraction we use $\mathcal{B}(f_1(1285) \to \eta\pi\pi) = 0.54 \pm 0.15$[1]

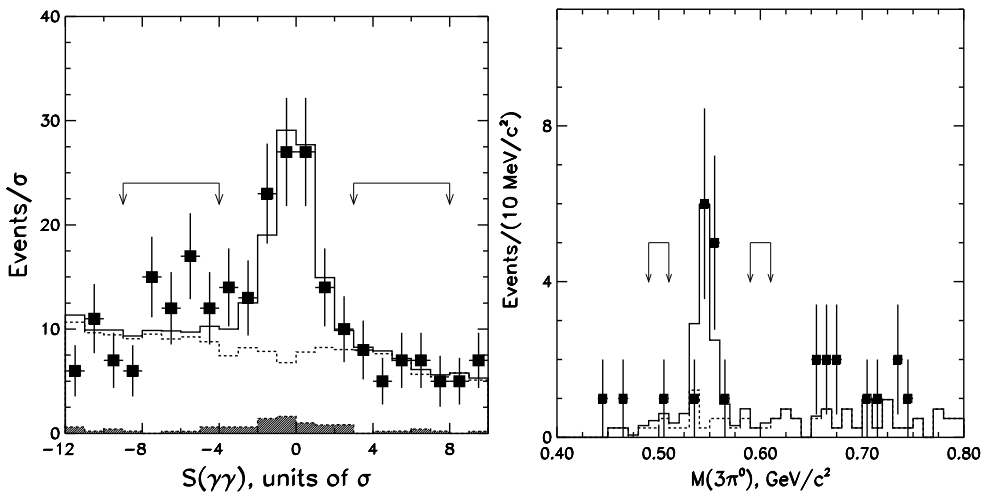

Figure 20: The η signals in the $\eta \to \gamma\gamma$ (left) and $\eta \to 3\pi^o$ (right) modes. For both plots the solid line is a fit including signal and random photon background (dashed line). The arrows indicate the range used for sideband subtraction. The contamination from $e^+e^- \to q\bar{q}$ events is given by the hatched area.

and the isospin prediction that $\eta\pi^+\pi^-$ is 2/3 of the $\eta\pi\pi$ state. We find:

$$\mathcal{B}(\tau^- \to f_1(1285)\pi^-\nu) = (6.0 \pm 1.7 \pm 2.1) \times 10^{-4}.$$

The second error quoted above is the systematic and it has components similar to the $\eta 3\pi$ analysis.

The decay $\tau^- \to f_1(1285)\pi^-\nu$ can also be present in 1-prong τ decays through $\tau \to \eta\pi^-\pi^o\pi^o\nu$. A sample of events consistent with this topology was isolated using similar π^o and η criteria as in the 3-prong case. In Fig 21 (top, right) the invariant mass of the $\eta\pi^o\pi^o$ system is plotted (1 entry per event). There is a clear enhancement at the $f_1(1285)$ mass. The scatterplot (Fig 21, bottom, right) of $m_{\eta\pi^o}$ vs. $m_{\eta\pi^o\pi^o}$ also resembles the 3-prong case as there appears to an enhancement at the $a_o(980)$ mass. The branching fraction extracted from this analysis is:

$$\mathcal{B}(\tau^- \to f_1(1285)\pi^-\nu) = (8.1 \pm 2.6 \pm 2.6) \times 10^{-4}.$$

This result is in good agreement with and independent of the 3-prong result. The two results can be combined to give:

$$\mathcal{B}(\tau^- \to f_1(1285)\pi^-\nu) = (6.7 \pm 1.4 \pm 2.2) \times 10^{-4}.$$

Using this result we find that a large component of $\tau^- \to \eta h^- h^+ h^- \nu$ contains an

$f_1(1285)$, i.e.

$$\frac{\mathcal{B}(\tau^- \to f_1(1285)\pi^-\nu)}{\mathcal{B}(\tau^- \to \eta h^- h^+ h^-\nu)} = 0.59 \pm 0.17.$$

These results have implications for CVC predictions for $\tau \to 6\pi\nu$ using $e^+e^- \to 6\pi$ data. The above results imply that $\tau \to 3\pi^{\pm}3\pi^o\nu$ and $\tau \to 5\pi^{\pm}\pi^o\nu$ have significant contributions from the $\tau \to \eta 3\pi\nu$ mode. Since this mode has G parity opposite to that of direct 6π decays and proceeds through the axial-vector current it must be subtracted before applying isospin or CVC to compare with e^+e^- annihilation data.

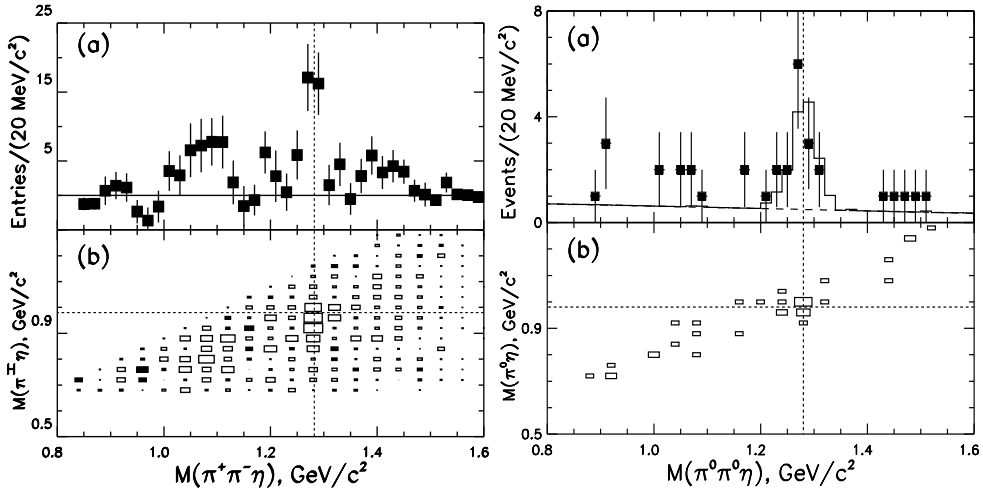

Figure 21: Mass of $\eta\pi^+\pi^-$ (a, left) and $\eta\pi^o\pi^o$ (a, right) system. Lower plots (b) are $M_{\eta\pi\pi}$ vs. $M_{\eta\pi}$. The dotted lines show the expected positions of the $f_1(1285)$ and $a_o(980)$ resonances.

3.2 Measurement of the Michel Parameters in Leptonic τ Decay

The leptonic decays of the τ, $\tau^- \to e^-\nu_\tau\bar{\nu}_e$ and $\tau^- \to \mu^-\nu_\tau\bar{\nu}_\mu$, can provide detailed information on the $\tau W\nu_\tau$ vertex. Since these decays are not clouded by the strong interaction they are ideal laboratories to explore the Lorentz structure of the $\tau W\nu_\tau$ current. Neglecting radiative corrections the distribution of the scaled energy ($x = E_l/E_{max}$) of the charged lepton in the τ rest frame can be written as:

$$\frac{1}{\Gamma}\frac{d\Gamma}{dx} = x^2 \frac{12(1-x) + \frac{4\rho}{3}(8x-6) + 24\eta m\frac{(1-x)}{x}}{1+4\eta m}$$

In the above equation ρ and η are the spectral shape Michel Parameters[34] and m is the scaled lepton mass $m = m_l/m_\tau$. In the standard model $\rho = 3/4$ and $\eta = 0$. At CLEO center of mass energies τ pairs are produced with no net polarization, hence the scaled energy spectrum is insensitive to the two other Michel Parameters, ξ and δ. It is important to measure ρ and η as accurately as possible, since non-standard electro-weak models predict values other than $\rho = 3/4$, $\eta = 0$. For example, $\eta \neq 0$ suggests the presence of a scalar boson that couples a right handed τ to a left handed l. Another example is the Two Higgs Doublet Model[35] with a charged Higgs. Here η_μ (measured using $\tau \to \mu\nu\bar{\nu}$) is related to the ratio of vacuum expectation values of the neutral components of the Higgs doublet (β) and the mass of the Higgs (m_H) by

$$\eta_\nu = -(m_\tau m_\mu tan^2\beta)/2m_H^2.$$

The sample of τ's used in this analysis were taken from $3.5fb^{-1}$ (3.2×10^6 τ pairs) of data collected at $E_{cm} \approx 10.6$ GeV. The decay mode $\tau^- \to h^-\pi^o\nu$ ($h^- = \pi^-,\ K^-$) was used as a tag in order to obtain a clean, high statistics sample of τ events.

Pairs of photons with polar angles (θ) satisfying $|cos\theta| < 0.71$ are used to form π^o's if their invariant mass is within 3σ of the nominal π^o mass. Electrons with momentum above 0.5 GeV/c are identified using a combination of dE/dx and tracking information from the drift chamber and energy measurements from the calorimeter. The background in this electron sample is estimated to be $(0.178 \pm 0.026)\%$. Muons with momentum above 1.5 GeV/c are identified as charged particles which are tracked through the inner and outer detector and pass through at least three absorbtion lengths of material. The background in this muon sample is estimated as $(1.08 \pm 0.16)\%$. Muons with momentum 0.5-1.5 GeV/c are identified by kinematically eliminating all other τ decay hypotheses ($\pi\nu$, $K\nu$, $e\nu\bar{\nu}$, $hn\pi^o\nu$). This muon sample contains a small amount of background from π/K, $h\pi^o\nu$, and $e\nu\bar{\nu}$ events ($\approx 4\%$ total).

The τ rest frame is the ideal Lorentz frame for simultaneously measuring ρ and η. CLEO, however, measures the momentum of the electrons and muons in the LAB frame. Unfortunately there is no unambiguous way to transform from the LAB frame to the τ rest frame due to the unmeasured neutrinos in the event. This lack of information can in part be compensated for using information from the "tag" τ. In the absence of initial or final state radiation the two τ's

in an event are produced back-to-back each with the energy of the beam. In a $\tau^- \to h^-\pi^o\nu$ decay the angle (α) between hadronic system ($H \equiv h\pi^o$) and the τ can be calculated using:

$$m_\tau^2 + m_H^2 - 2E_\tau E_H + 2p_\tau p_H cos\alpha = m_\nu^2.$$

In the above equation E_H, p_H, and m_H are calculated quantities while we assume $m_\nu = 0$ and $E_\tau = E_{beam}$. As $cos\alpha \to 1$ the ambiguity in ϕ disappears and the momentum vector of the $h\pi^o$ system gives a good estimate of the $\tau \to l\nu\bar{\nu}$ direction. Thus events with $cos\alpha > 0.970$ are used to transform the lepton momentum spectra to a pseudo rest frame (PRF). After the $cos\alpha$ cut there are 18587 electrons and 12580 (2931) high momentum (low, $p < 1.5$ GeV/c) muons left in the sample. The x spectrum for electrons and muons passing all cuts is shown in Fig. 22. In order to extract η and ρ values from the data a χ^2 fit is performed

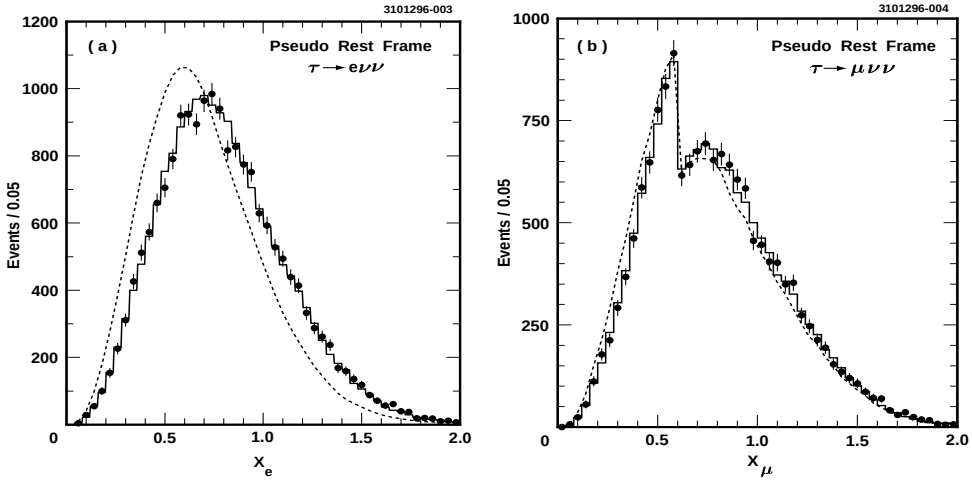

Figure 22: Scaled energy spectrum (x) for electrons (a) and muons (b) in the pseudo rest frame of the τ. The dotted line in (a) is a $V + A$ Monte Carlo calculation, while the dotted line in (b) is a Monte Carlo calculation of the muon spectrum assuming $\eta = 1$. Events with $x > 1$ are the result of imperfect reconstruction of the τ direction. The discontinuity in (b) at $x = 0.6$ is due to low momentum muons.

using three binned Monte Carlo x spectrums. The three individual x spectrums are generated with (ρ, η) values: (3/4,0), (0,0), and (3/4,1). The data spectrum is then represented by:

$$N\frac{dN}{dx}(\rho,\eta) = N_{3/4,0}\epsilon_{V-A}\frac{dN}{dx}(3/4,0) + N_{0,0}\epsilon_{V+A}\frac{dN}{dx}(0,0) + N_{3/4,1}\epsilon_{\eta=1}\frac{dN}{dx}(3/4,1)$$

Table 15: CLEO results along with the corresponding previous world average results.

Parameter	CLEO II	World Average
ρ_e^τ	0.732±0.014 ± 0.009	0.736±0.028
ρ_μ^τ	0.747±0.048 ± 0.044	0.74±0.04
η_μ^τ	0.010±0.149 ± 0.171	-0.24±0.29
$\rho_{e\mu}^\tau$	0.735±0.013 ± 0.008	0.742±0.027
$\eta_{e\mu}^\tau$	-0.015±0.061 ± 0.062	-0.01±0.14

with:

$$N = N_{(3/4,0)} + N_{(0,0)} + N_{(3/4,1)} = \frac{4\rho/3 - \eta}{1 + 4\eta m} + \frac{1 - 4\rho/3}{1 + 4\eta m} + \frac{\eta(1 + 4m)}{1 + 4\eta m}.$$

The ϵ's are efficiency corrections for each Monte Carlo x spectrum. The τ Monte Carlo spectrums are generated using the simulation packages KORALB,[32] TAUOLA,[33] and PHOTOS.[36] The CLEO II detector is simulated using GEANT.[7] All effects due to radiation, resolution, and efficiency are included in these spectra. The events which passed the $cos\alpha$ cut are analyzed in the PRF frame. An additional 12981 (9186) electron (muon) events which do not satisfy the $cos\alpha$ cut are analyzed in the LAB frame.

The results from fitting the spectra are given in Table 15. A detailed study of systematic errors leads to the uncertainties quoted in this Table. Using lepton universality a simultaneous fit to the electron and muon data is performed resulting in the values of $\rho_{e\mu}^\tau$ and $\eta_{e\mu}^\tau$ given in Table 15. In Fig. 23 the results from the individual and combined modes are displayed as well as the prediction from the standard model. All measurements are consistent with a $V - A$ Lorentz structure for the current in τ decay. In Fig. 24 the CLEO results along with other measurements of ρ and η are presented. The CLEO results are consistent with, but more precise than previous measurements. Finally, the measurement of η leads to the model dependent limit on the charged Higgs mass of $M_{H^\pm} > (0.97 \times tan\beta)$ GeV at the 90% confidence level.

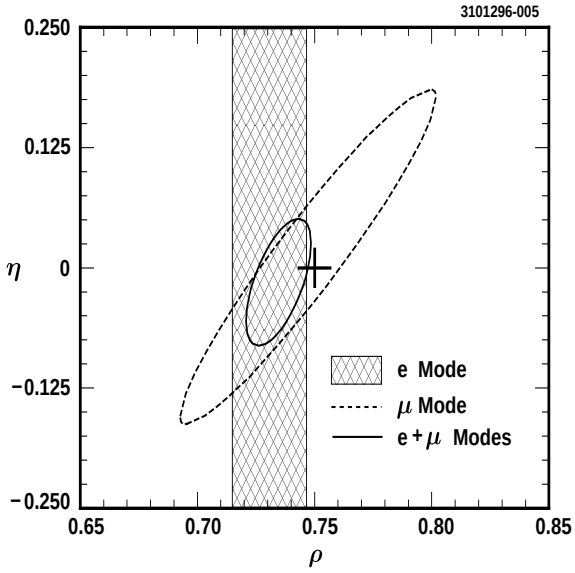

Figure 23: ρ *vs.* η for electron, muon and combined modes. The standard model prediction is given by the cross.

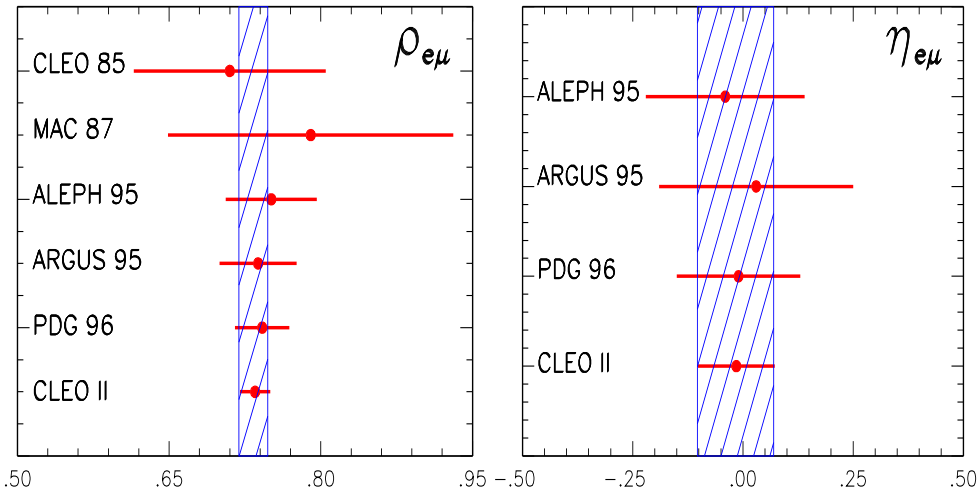

Figure 24: Results for the Michel parameters $\rho_{e\mu}$ and $\eta_{e\mu}$.

3.3 Search for $\tau \to e^-\gamma$ and $\tau \to \mu^-\gamma$

The standard model does not contain a symmetry associated with lepton number. Therefore one expects that lepton number violating decays should be present in nature. Clearly the rate of these decays is small as shown by the experimental upper limits[1] for lepton number violation in muon decay ($\mathcal{B}(\mu \to e\gamma) < 4.9 \times 10^{-11}$, $\mathcal{B}(\mu \to eee) < 1 \times 10^{-12}$). Although it is not possible to collect τ data samples comparable to those used to obtain the limits from muon decay there are reasons to use τ's as a probe of lepton number violation. For example, there are models which relate lepton number violation to mass dependent couplings. One such model[37] favors τ decay and predicts an enhancement of $\mathcal{B}(\tau \to \mu\gamma) = 2 \times 10^5 \mathcal{B}(\mu \to e\gamma)$.

Lepton number violation in τ decay has been studied extensively for close to two decades now. The 1996 version of the Review of Particle Properties[1] gives limits on 37 different lepton number violating τ decay modes. The most stringent limit in the list is a result from CLEO,[38] $\mathcal{B}(\tau \to \mu\gamma) < 4.2 \times 10^{-6}$. Here we update this CLEO result and present a new upper limit for $\mathcal{B}(\tau \to e\gamma)$.

The data in this analysis consists of 4.68 fb^{-1} ($\approx 4.24 \times 10^6 \tau^+\tau^-$ pairs) of data taken at energies at and slightly below the mass of the Υ(4S). Events that are consistent with the 1 vs. 1 topology (i.e. oppositely charged tracks in different hemispheres) are kept for further consideration. Requirements on the tag hemisphere are minimal and all standard 1-prong τ decays are used. Event selection criteria were developed from a study of Monte Carlo events incorporating both KORALB[32] and GEANT.[7]

This analysis relies heavily on lepton (electron and muon) identification both for isolating a signal and rejecting background. The standard CLEO lepton identification software package is used here. Electrons are identified with a combination of calorimeter, drift chamber tracking and dE/dx, and time of flight information. Identified muons are charged tracks that are tracked from the inner drift chambers all the way through the magnet iron. Since radiative bhabhas and μ-pairs are backgrounds to this analysis events can have only one identified electron or one identified muon.

Additional background suppression is achieved by examining both the missing momentum and transverse momentum in the event. Since there must be at least one undetected neutrino on the tag side of the event the missing momentum in

Table 16: Efficiencies, observed events (n_o), background events (μ_B), calculated number of events including systematic error for 90% confidence level upper limits (λ), and the 90% confidence level upper limits for $\tau \to e\gamma$ and $\tau \to \mu\gamma$.

Channel	MC efficiency	n_o	μ_B	λ	Upper limit at 90% CL
$\tau \to e\gamma$	10.1	0	2.0	2.3	2.7×10^{-6}
$\tau \to \mu\gamma$	14.4	3	5.5	3.7	3.0×10^{-6}

a τ event should lie in the tag hemisphere. However, the missing momentum in QED background processes will be randomly oriented with respect to the "tag" track. Thus only events where the cosine of the angle between the tag track's momentum vector and the missing momentum vector is greater than 0.4 are kept for further study. A cut on transverse momentum ($p_{trans} > 0.3$GeV/c) is made to eliminate backgrounds from the 2-photon process.

The events that pass all selection criteria are shown in Fig. 25. The signature for $\tau \to e\gamma$ or $\tau \to \mu\gamma$ is an $l\gamma$ combination with measured energy and invariant mass consistent with the beam energy and τ mass respectively. For convenience the variables $\Delta E = E_{l\gamma} - E_{beam}$ and $m_{l\gamma} - m_\tau$ are used in this analysis. The central box in both plots of Fig. 25 shows the signal region in the $(\Delta E, m_{l\gamma})$ plane. The boundaries of the signal region were determined using a Monte Carlo simulation (two body phase space) of the decays $\tau \to e\gamma$, $\tau \to \mu\gamma$ (open circles in Fig. 25). There are no candidate events for the $e\gamma$ channel and three candidates for the $\mu\gamma$ channel. From a study of the sideband regions in Fig. 25 2 (5.5) background events are predicted for the $e\gamma$ ($\mu\gamma$) channel. A Monte Carlo study suggests that the $\mu\gamma$ background events originate from generic τ decays. The results of the analysis are summarized in Table 16. The upper limits presented here include systematic uncertainties calculated according to the prescription of Cousins and Highland.[39] Thus the strictest limit on lepton number violation in τ decay now belongs to the $e\gamma$ mode.

4 Future Plans, CLEO III

The CLEO experiment is currently taking data at the $\Upsilon(4S)$ with a recently (summer 1995) installed three layer silicon vertex detector. Data taking with this

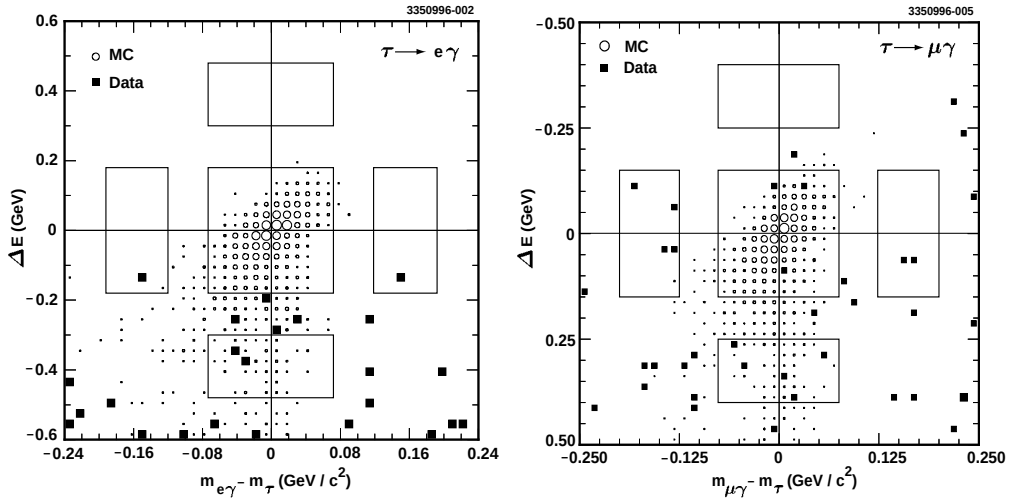

Figure 25: The ΔE vs. $m_{l\gamma} - m_\tau$ distributions for $\tau \to e\gamma$ and $\tau \to \mu\gamma$. The solid squares are the data while the open circles are the Monte Carlo signal events.

detector configuration is expected to continue until early 1998 when the experiment and CESR will shut down for major renovation. Installed in place of the present detector will be CLEO III (Fig. 26). This detector features a new silicon vertex detector (4 layers), a new main drift chamber, and a ring imaging Čerenkov detector (RICH). The present calorimeter, magnet, and muon detector are also used in this version of CLEO. The main advantage of CLEO III over CLEO II is in the area of particle identification. The RICH detector should be able to provide $\geq 3\sigma$ π/K separation over the entire momentum region of interest for $B-$meson decay. Upgrades to CESR should put the instantaneous luminosity in excess of $10^{33} cm^{-2} s^{-1}$. This combination of detector and accelerator will increase the physics reach of CLEO by over an order of magnitude in the areas of b, c, and τ physics. In fact, it may even allow for the first observation of CP violation in the $b-$quark sector.

5 Acknowledgements

It is a pleasure to acknowledge the efforts of my colleagues in the CLEO collaboration and the staff of CESR. A special word of thanks to the many people who made the SLAC Summer Institute a most enjoyable experience.

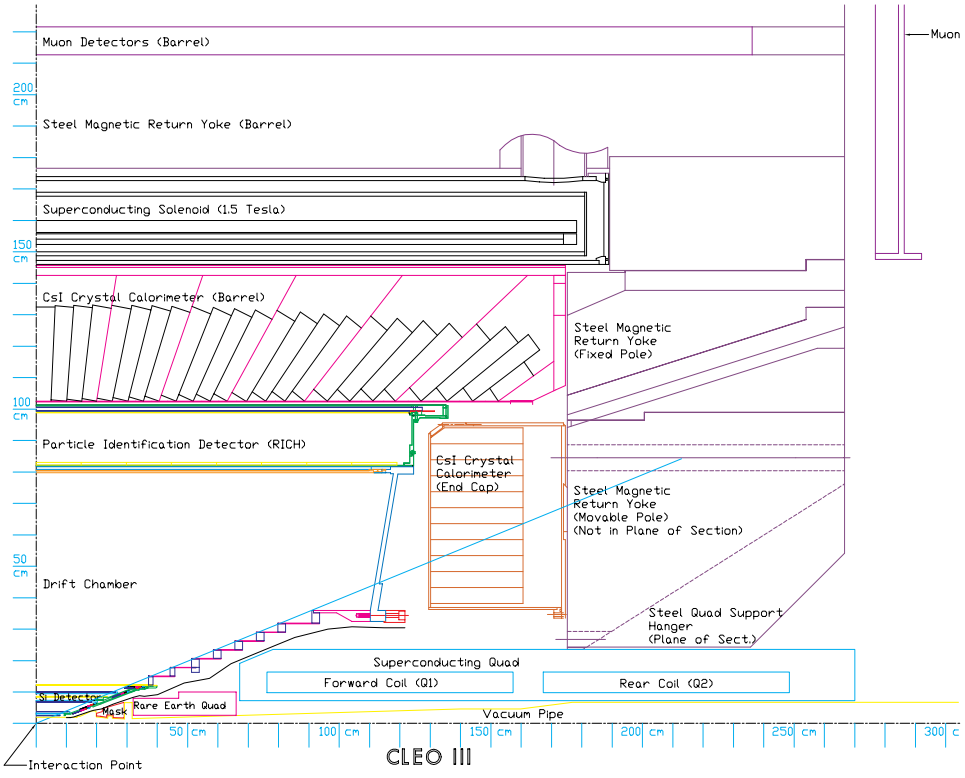

Figure 26: Quarter section of the CLEO III detector.

References

[1] Particle Data Group, R. Barnett, *et al.*, Phys. Rev. D **54**, 1 (1996).

[2] Y. Kubota *et al.*, Nucl Inst. Meth. **320**, (1992) 66.

[3] R. Aleksan, *et al.*, Phys. Lett. B**317**, 173 (1993), The *BaBar* Collaboration, TDR, SLAC-R-95-457 (1995), K. Lingel, *et al.*, "Physics Rationale for a B Factory", CLNS-91-1043 (1991).

[4] D. Gibaut, *et al.*, Phys. Rev. D**53**, 4734 (1996).

[5] G. Eilam, *et al.*, Phys. Rev. Lett. **74**, 4984 (1995).

[6] N. G. Deshpande, *et al.*, Phys. Rev. D **52**, 5354 (1995).

[7] R. Brun, *et al.*, CERN dd/ee/84-1.

[8] ALEPH Collaboaration, in Proceedings of the International Conference on High Energy Physics, Warsaw, 1996 (Report No. PA-05-057).

[9] P. Avery, *et al.*, Phys. Lett. B**223**, 470 (1989).

[10] DELPHI Collaboaration, W. Adam, *et al.* (to be published).

[11] R. Ammar, *et al.*, Phys. Rev. Lett. **71**, 674 (1993).

[12] T. Altomari, Phys. Rev. D **37**, 677 (1988); N. G. Deshpande, *et al.*, Z. Phys. C **40**, 369 (1988); C. A. Dominguez, *et al.*, Phys. Lett. B**214**, 459 (1988); N. G. Deshpande and J. Trampetic, Ann. N. Y. Acad. Sci., **578**, 424 (1989); T. M. Aliev, *et al.*, Phys. Lett. B**237**, 569 (1990); A. Ali and T. Mannel, Phys. Lett. B**264**, 447 (1991); R. N. Faustov and V. O. Galkin, Mod. Phys. Lett. A**7**, 2111 (1992); A. Ali, T. Ohl and T. Mannel, Phys. Lett. B**298**, 195 (1993); El hassan El aaoud and Riazuddin, Phys. Rev. D **47**, 1026 (1993); P. Colangelo, *et al.*, Phys. Lett. B**317**, 183 (1993); P. J. O'Donnell and H. K. K. Tung, Phys. Rev. D **48**, 2145 (1993); A. Ali and C. Greub, Z. Phys. C **60**, 433 (1993); P. Ball, TUM-T31-43/93; A. Ali, V. M. Braun and H. Simma, Z. Phys. C **63**, 437 (1994); C. Bernard, P. Hsieh and A. Soni, Phys. Rev. Lett. **72**, 1402 (1994); B. Holdom and M. Sutherland, Phys. Rev. D **49**, 2356 (1994); S. Narison, Phys. Lett. B**327**, 354 (1994); K. C. Bowler, *et al.*, Edinburgh-94-544 (1994); M. Ciuchini, *et al.*, Phys. Rev. D**51**, 137 (1994); J. Tang, *et al.*, Phys. Rev. D**51**, 3501 (1995).

[13] M. S. Alam, *et al.*, Phys. Rev. Lett. **74**, 2885 (1995).

[14] J. M. Soares, Phys. Rev. D **49**, 283 (1994).

[15] C. Greub, H. Simma, and D. Wyler, Nucl. Phys. B **434**, 39 (1995).

[16] A. Ali, V. M. Braun and H. Simma, Z. Phys. C **63**, 437 (1994).

[17] S. Narison, Phys. Lett. B**327**, 354 (1994).

[18] D. Buskulic, *et al.*, Phys. Lett. B**356**, 409 (1995).

[19] R. Grigjanis, P. J. O'Donnell, M. Sutherland, and H. Navelet, Phys. Lett. B**224**, 209 (1989).

[20] N. G. Deshpande, X.-G. He, and J. Trampetic, Phys. Lett. B**377**, 161 (1996).

[21] L.-L. Chau, *et al.*, Phys. Rev. D**43**, 2176 (1991); A. Deandrea, *et al.*, Phys. Lett. B**318**, 549 (1993); A. Deandrea, *et al.*, Phys. Lett. B**320**, 170 (1994); D. Du and L. Guo, BIHEP-TH-95-28.

[22] R. Fulton, *et al.*, Phys. Rev. Lett. **64**, 16 (1990); J. Bartelt, *et al.*, Phys. Rev. Lett. **71**, 4111 (1993).

[23] H. Albrecht, *et al.*, Phys. Lett. B**234**, 409 (1990); **255**, 297 (1991).

[24] N. Isgur and D. Scora, Phys. Rev. D **52**, 2783 (1995).

[25] M. Wirbel, B. Stech, and M. Bauer, Z. Phys. C **29**, 637 (1985).

[26] J. G. Körner and G. A. Schuler, Z. Phys. C **38**, 511 (1988).

[27] D. Melikhov, Phys. Rev. D **53**, 2460 (1996).

[28] G. Burdman and J. Kambor, FNAL Report No. FERMILAB-Pub-96/033-T, 1996; J. M. Flynn, *et al.*, Nucl. Phys. **B461**, 327 (1996); B. Stech, Phys. Lett. B**354**, 447 (1995).

[29] M. Artuso, *et al.*, Phys. Rev. Lett. **69**, 3278 (1992).

[30] J. Bartelt, *et al.*, Phys. Rev. Lett. **76**, 4119 (1996).

[31] A. Pich, Phys. Lett. B**196**, 561 (1987).

[32] S. Jadach and Z. Was, Comp. Phys. Commun. **64**, 267 (1991); S. Jadach, *et al.*, Comp. Phys. Commun. **76**, 361 (1993).

[33] S. Jadach, J. H. Kuhn and Z. Was, CERN-TH-5856/90 (1990).

[34] L. Michel, Proc. Phys. Soc. London A **63**, 514 (1950).

[35] A. Stahl, Phys. Lett. B**324**, 121 (1994).

[36] E. Barberio, B. van Eijk and Z. Was, CERN-TH-5857/90 (1990).

[37] R. Arnowitt and P. Nath, Phys. Rev. Lett. **66**, 2708 (1991).

[38] J. Bartelt, *et al.*, Phys. Rev. Lett. **73**, 1890 (1994).

[39] R. Cousins and V. Highland, Nucl. Instr. and Meth. A**320** 331 (1992).